



A space-time upscaling technique for modeling high-cycle fatigue-damage of short-fiber reinforced composites

Nicola Magino^a, Jonathan Köbler^a, Heiko Andrä^a, Fabian Welschinger^b, Ralf Müller^c,
Matti Schneider^{d,*}

^a Fraunhofer ITWM, Department of Flow and Material Simulation, Germany

^b Robert Bosch GmbH, Corporate Sector Research and Advance Engineering, Germany

^c TU Darmstadt, Division of Continuum Mechanics, Germany

^d Karlsruhe Institute of Technology (KIT), Institute of Engineering Mechanics, Germany

ARTICLE INFO

Keywords:

High-cycle fatigue damage
Stiffness degradation
Short-fiber reinforced materials
Mean-stress dependence
Cycle jump

ABSTRACT

Characterizing short-fiber reinforced polymers under high-cycle fatigue loading is a tedious experimental task. To reduce the necessary experiments to a minimum, we introduce a computational strategy involving a mean-stress dependent fatigue-damage model for the stiffness degradation in short-fiber reinforced polymers. The key challenge in these materials is their inherent anisotropy which makes the necessary mechanical characterization process rather time-intensive, in particular for long-time experiments required for fatigue tests. Computational multiscale approaches may reduce the necessary mechanical tests to a bare minimum, offering significant savings in expense.

We propose a mean-stress sensitive model to simulate the stiffness degradation in short-fiber reinforced composites subjected to fatigue loading. We start with a model formulated in time space and provide a multiple-scale-bridging approach to arrive at a computationally efficient effective model. For a start, we describe a high-accuracy cycle-jump technique which permits us to simulate a large number of cycles, required for high-cycle fatigue. In a second step, we apply a model-order reduction in space to arrive at an effective model on component scale. Finally, we rely upon a fiber-orientation interpolation technique to produce an effective material model which covers all relevant fiber-orientation states throughout the component.

Our approach utilizes a recently introduced compliance-based damage model for describing the stiffness degradation of the matrix material. We demonstrate the capability of the computational multiscale model to reproduce the stiffness degradation in fatigue experiments for different orientations, stress amplitudes, stress ratios between $R = -1$ and $R = 0$ and geometries with different notches.

1. Introduction

1.1. State of the art

Short-fiber reinforced thermoplastic materials are of central importance in lightweight constructions. The experimental characterization and the numerical prediction of their mechanical behavior have thus been under extensive research over the last decades. Polymer materials show a complex material behavior [1] that is influenced by the reinforcements' geometry (like aspect ratio and orientation) [2,3] which depends on environmental conditions like temperature [4] and humidity [5,6], and includes notch effects [7,8]. Due to the dependence of the

local fiber orientations on the injection-molding process, the composite material inherits different anisotropic behavior at every material point of the macroscale component, in general.

The fatigue behavior of thermoplastic materials is different from the rather well understood metallic materials. In contrast to metals, under fatigue loading thermoplastic materials show a significant stiffness decrease prior to failure [9,10]. This stiffness decrease depends on the fiber orientation and the stress amplitude. To the authors' knowledge, there is little literature available on the effect of the mean stress on the stiffness degradation in short-fiber reinforced polymers or pure thermoplastics [11]. Amjadi et al. [12] studied damage in thermoplastics under multi-axial fatigue loading in depth. They observed that mean

* Corresponding author.

E-mail address: matti.schneider@kit.edu (M. Schneider).

stress has no significant effect on *failure* under cyclic torsion, whereas mean stresses in cyclic shear significantly influence the life time of the specimen. They suggested using a critical plane based fatigue parameter sensitive to mean normal stress acting on the critical plane. Berrehili et al. [13,14] performed fatigue experiments with different mean stresses on high-density polyethylene (HDPE) and polypropylene (PP). They found the commonly known Sines [15] and Crossland [16] criteria (dependent on hydrostatic and equivalent von Mises stress) to be insufficient in capturing mean stress effects observed for HDPE. Instead, they proposed a criterion solely dependent on the von Mises norm of the mean and the maximum stress that was able to reproduce the failure of HDPE under tensile fatigue loading in tension, torsion, compression and combined tension-compression. Zhang et al. [17] discuss equivalent stress measures for multi-axial loading in polymers. For short-fiber reinforced materials, Launay et al. [18,19] performed an extensive study comparing multiple multi-axial fatigue criteria from the literature and a proposed energy dissipation criterion for data of PA66-GF35. Besides the energy dissipation criteria, the Sines criterion was shown to meet the experimental data quite well. Klimkeit et al. [20] recommend an energy-based criterion in the context of Through Process Modeling (TPM), a method in which fatigue failure is predicted based on the elastic undamaged material behavior [21]. De Monte et al. [22] observed that the slopes in Wöhler curves are not significantly influenced by different loading conditions, with torsion curves slightly flatter than tension curves and no observable difference in the slope for Wöhler curves of different mean stresses. The same authors studied the hysteresis evolution of short-fiber reinforced polyamide 6.6 under fatigue at different mean stresses [11,23]. For stress ratios $R = 0$ (defined as $R = \sigma_{\min}/\sigma_{\max}$), mean ratcheting is more pronounced than for mean-stress free experiments.

The influence of notches on the fatigue life of short-fiber reinforced polymers has been investigated by several authors. Zhou and Mallick [24] studied fatigue specimens with holes of varying radius. The diameters ranged from 1.58 mm to specimens without a hole. They observed that the fatigue life of the specimen is independent of the hole's radius, provided the nominal stress is used. Sonsino and Moosbrugger [8] analyzed different notch geometries from an unnotched specimen to sharply notched (notch radius of 0.2 mm). They observed that with increasing sharpness of the notch, the fatigue life of the specimen decreases w.r.t. the nominal stress. These results, which appear contradicting at first glance, may be a result of different notch geometries used - Zhou and Mallick [24] used circular holes, whereas Sonsino and Moosbrugger [8] prepared slits. Bernasconi et al. [25] reported a decrease in fatigue life with decreasing notch radius.

In the context of modeling material degradation, the continuum damage approach [26,27] has been applied widely. Here, the material degradation is considered as a process depending on internal variables, whose evolution equations in time have to be determined to match experiments.

In the context of fatigue simulations, progressive damage models may be classified into two categories. In the first one, the evolution of the material is directly formulated in cycle space, i.e., the time variable t is replaced by a dimensionless time-like variable N accounting for the current cycle [28–30]. The second approach consists of kinetic models formulated in time space. These models have the advantage that they account for changes in the load cycle path in a direct and consistent manner. However, this comes at the cost of a drastic reduction of the numerical efficiency as the load path during each cycle has to be resolved rather accurately. To reduce this computational burden, different strategies were developed. For cycle-jump techniques [31,32], the material behavior is computed for a few cycles, and the evolution for future cycles is extrapolated. Several authors used this approach in the context of composite structures [33–35]. Titscher and Unger [36] recently published an extension to high-order integration schemes. Bhattacharyya et al. [37] combined a cycle jump approach with temporal homogenization for combined cyclic fatigue. Another possible

approach is the large time increment method (LATIN) which was applied to complex material behavior like viscoplasticity [38] and fatigue damage governed by microplasticity in metals [39]. This strategy becomes particularly powerful when combined with the Proper Generalized Decomposition [40] (PGD) at the global (macroscopic) stage [41]. As a third approach, two-time-scale averaging methods offer a possibility to study the influence of the fast-scale loading in an analytical, parametrized way [42–44] provided the loading profiles on the faster time scale are known a priori. Devulder et al. [45] applied this technique to fatigue damage.

Due to the dependence on the local fiber orientation, predicting the effective material behavior of short-fiber materials is challenging. Computational homogenization techniques based on Fast Fourier Transformation (FFT), introduced by Moulinec and Suquet [46], are frequently used due to their accuracy and flexibility in computing the effective response of microstructures. For short-fiber reinforced polymers, coupled FE-FFT-methods [47] were successfully applied to damage simulations [48].

Model-order reduction techniques offer a possibility to further alleviate the computational burden of fully coupled micro-macro simulations, e.g., the transformation field analysis (TFA) originally proposed by Dvorak [49] and its non-uniform extension [50,51]. Köbler et al. [52] successfully applied this method in the context of fatigue damage of short-fiber reinforced polymers. Alternatively, machine learning techniques can be employed [53–56].

1.2. Contributions

In this work, we propose a fatigue-damage model for the matrix material in short-fiber reinforced polymers formulated in the time scale. This model may be regarded as an extension of the rate-independent convex damage model proposed by Görthofer et al. [57] to fatigue damage. Similar to approaches of Köbler et al. [52] and Jain et al. [58], we are interested in the stable stiffness degradation of the material observed prior to failure. In contrast to these models, we chose a formulation of the damage material law in time space rather than cycle space. Building upon the work of Paas et al. [59] and Peerlings [60], the proposed material evolution only increases damage under loading (in contrast to unloading). One of the main advantages of a damage model formulated in time-space is the consistent incorporation of changes in the loading path into the material-evolution equations. Indeed, changes in mean stress values or the wave form directly influence the material behavior. Their main disadvantage however is the possibly very large computational costs for computations in the high-cycle regime.

To combine the advantages of both approaches, we propose a cycle-jump technique building upon parametric loading curves. In fatigue experiments, the wave form of the loading path is known a priori. A parametrization of the wave form enables us to reformulate the time-scale model in cycle space and, subsequently, a logarithmic cycle space. As the mechanical experiments in the work at hand have a sinusoidal wave form, we discuss this case in detail.

We obtain related fatigue-damage models formulated in three time-like scales: time space, cycle space and *logarithmic* cycle space. We thoroughly discuss approximations and resulting regimes of applicability in section 3. In the high-cycle regime, the logarithmic cycles scale is applicable and allows for very large steps in cycle steps, reducing the computational effort significantly.

The obtained logarithmic cycle scale may be viewed as an extension of the compliance-based fatigue damage model [61] using an effective stress depending on the parametrized wave form. It thus extends the former model to computations at different mean stress values. Incidentally, this point of view enables us to make use of the model-order reduction technique based on a reformulation of the equations in terms of the stress proposed in a recent work of the authors [61]. We study the accuracy of model-order reduction technique for a commercial polyamide material.

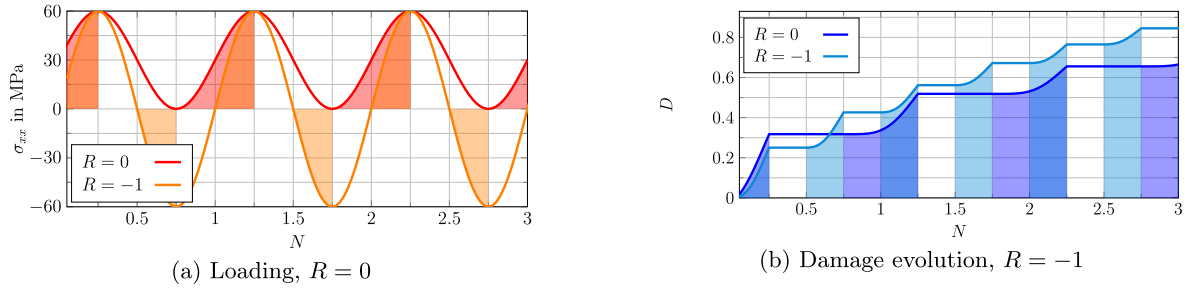


Fig. 1. Damage evolution under cyclic loading of a homogeneous material.

Last but not least, we demonstrate the capability of the model to predict the stiffness degradation of a short-fiber reinforced polymer at different stress amplitudes, stress ratios, orientation states and geometries. Using only one material parameter, the fatigue damage evolution speed α , we can show that the material behavior of the composite under these various loading scenarios is predicted with reasonable accuracy sufficient for industrial applications.

Notation

Scalars are denoted by non-bold letters, whereas bold letters are reserved for vectors and second-order tensors. Fourth-order tensors are denoted by double-stroke bold symbols, e.g., \mathbb{C} or \mathbb{S} . Tensor contraction is denoted by \cdot , and we use: for a double contraction.

2. The fatigue-damage model in time

We introduce a damage material based on a free energy density

$$w(\boldsymbol{\epsilon}, D) = \frac{1}{2} \frac{1}{1+D} \boldsymbol{\epsilon} : \mathbb{C}_0 : \boldsymbol{\epsilon} \quad (2.1)$$

with a scalar damage variable $D \geq 0$, an undamaged stiffness tensor \mathbb{C}_0 and the strain tensor $\boldsymbol{\epsilon}$. Using a damage variable and a suitable free energy potential is a rather typical strategy in continuum damage mechanics [62]. However, the form of the damage model is non-standard. It may be considered as an adaption of the damage model introduced by Görthofer et al. [63] to fatigue loading. The corresponding stress is derived from the energy density by

$$\boldsymbol{\sigma} \equiv \frac{\partial w}{\partial \boldsymbol{\epsilon}}(\boldsymbol{\epsilon}, D) = \frac{1}{1+D} \mathbb{C}_0 : \boldsymbol{\epsilon}. \quad (2.2)$$

The associated damage-driving force computes as

$$Y_D \equiv -\frac{\partial w}{\partial D}(\boldsymbol{\epsilon}, D) = \frac{1}{2} \frac{1}{(1+D)^2} \boldsymbol{\epsilon} : \mathbb{C}_0 : \boldsymbol{\epsilon}. \quad (2.3)$$

Note that for a linearization of $1/(1+D)$ around the undamaged state, the stress strain relationship matches the Lemaitre model [64]. We may express the driving force Y_D as a function of the stress $\boldsymbol{\sigma}$ and the internal variable D

$$Y_D(\boldsymbol{\sigma}, D) = \frac{1}{2} \boldsymbol{\sigma} : \mathbb{S}_0 : \boldsymbol{\sigma} \quad (2.4)$$

with the compliance tensor $\mathbb{S}_0 = \mathbb{C}_0^{-1}$ of the undamaged state. Paas et al. [59] and Peerlings [60] introduced phenomenological models to capture the effects of fatigue damage. They proposed a damage evolution law where damage only increases under positive loading, i.e., whenever a carefully chosen equivalent strain measure ϵ_{eq} was increasing, i.e., the condition $\dot{\epsilon}_{\text{eq}} > 0$ holds. Suiker et al. [65] used a similar approach in the context of cyclic plasticity.

We follow this line of reasoning and consider the damage-driving force Y_D as an equivalent strain measure. More precisely, we define

$$\dot{D}(\boldsymbol{\epsilon}, D, q) = \begin{cases} \alpha_q(q) Y_D(\boldsymbol{\epsilon}, D), & \text{if } \dot{Y}_D(\boldsymbol{\epsilon}, D) \geq 0, \\ 0, & \text{otherwise.} \end{cases} \quad (2.5)$$

here, α_q denotes a (time-dependent) material parameter which governs the speed of damage evolution. Similar to Largeton et al. [66], who considered the effect of aging onto viscoelastic properties, we introduce a variable q to model the cycle dependence of the material parameter via the empirical relationship

$$\alpha_q(q) = \frac{4\alpha_t}{q} \quad (2.6)$$

with a parameter $\alpha_t > 0$. The variable q is assumed to grow at a constant rate

$$\dot{q} = K_t \quad (2.7)$$

with some scalar parameter K_t . The evolution equation (2.7) for q can be integrated explicitly. For a fixed duration of a load cycle $T > 0$, we express the (global) time t as the superposition of a cycle-count variable $N \geq 0$ and a sub-cycle variable $\tau \in [0, 1]$

$$t = T(N + \tau). \quad (2.8)$$

For the initial condition $q(t=0) = q_0$, we obtain the expression

$$q = q_0 + K_t t \equiv q_0 + K(N + \tau) \quad (2.9)$$

in terms of the parameter $K = K_t T$ for constant duration of a single load cycle T . The model at hand permits damage to grow only during loading. The latter is characterized by the condition $\dot{Y}_D > 0$. To demonstrate the behavior of the material model, we consider an exemplary isotropic matrix material with Young's modulus $E = 3.35$ GPa, Poisson's ratio $\nu = 0.4$ and material-model parameters $\alpha_t = 0.1$ 1/MPa, $K = 5.0$ as well as $q_0 = 5.0$. The material is subjected to a sinusoidal loading for uniaxial stress-driven tension in x-direction. The load curves are shown in Fig. 1 (a) for two different stress ratios R , defined by $R = \sigma_{\text{min}}/\sigma_{\text{max}}$, namely $R = 0$ and $R = -1$. The peak stress in both cases is $\sigma_{\text{max}} = 60$ MPa. The corresponding damage evolutions are shown in Fig. 1(b). Damage only increases for a positive loading rate $\dot{Y}_D \geq 0$. Comparing the different load cases after 3 load cycles in Fig. 1(b), we observe that for same maximum stress σ_{max} , the damage evolution for a stress ratio of $R = -1$ is faster than for $R = 0$.

We complete the discussion with several remarks: For a start, the proposed model is thermodynamically consistent. Indeed, the dissipation for isothermal, small-strain systems [[67], Chapter 5.3] computes as

$$\begin{aligned} \mathcal{D} &\equiv \boldsymbol{\sigma} : \dot{\boldsymbol{\epsilon}} - \dot{w} = \boldsymbol{\sigma} : \dot{\boldsymbol{\epsilon}} - \frac{\partial w(\boldsymbol{\epsilon}, D)}{\partial D} \dot{D} - \frac{\partial w(\boldsymbol{\epsilon}, D)}{\partial \boldsymbol{\epsilon}} : \dot{\boldsymbol{\epsilon}} \\ &= \begin{cases} \alpha_q(q) Y_D(\boldsymbol{\epsilon}, D)^2, & \text{if } \dot{Y}_D(\boldsymbol{\epsilon}, D) \geq 0, \\ 0, & \text{otherwise.} \end{cases} \end{aligned} \quad (2.10)$$

This is always positive for

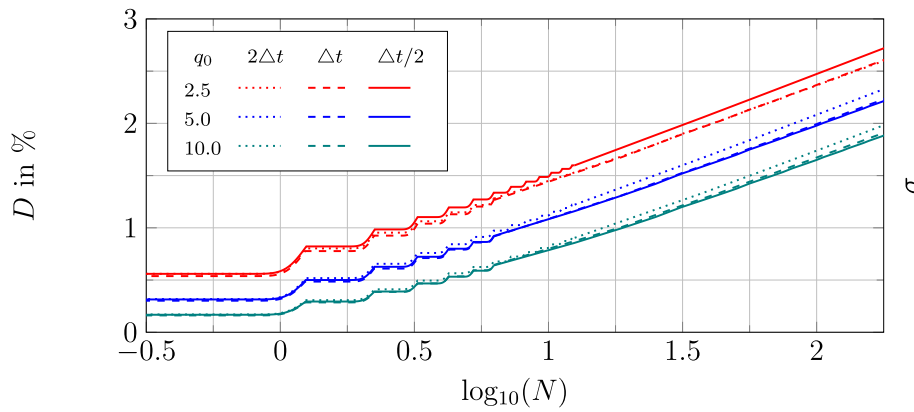


Fig. 2. Time-resolution study for the fatigue-damage model.

$$\alpha_q(q) = \frac{4\alpha_\tau}{q_0 + K(N + \tau)} \geq 0. \quad (2.11)$$

Thus, the dissipation \mathcal{D} is non-negative, i.e., thermodynamic consistency holds. Secondly, the free energy of the material model is jointly convex in the variables ϵ and D . Thus, the model does not permit localization and allows to compute mesh-insensitive results without regularization methods pertinent in continuum damage models [68–70]. For a more in-depth discussion, we refer to Görthöfer et al. [57]. In the context of efficient simulation of cyclic loading, this comes with another advantage. In localizing fatigue models, cycle-jump techniques critically depend on an accurate adaptive step-size selection-strategy [71]. Non-localizing models are more robust and thus expected to be less sensitive w.r.t. the chosen cycle-jump size. Clearly, as damage localization is excluded, the applicability of the model is inherently limited to stable, non-localized damage corresponding to the range of stable stiffness degradation prior to failure under fatigue loading. A model permitting damage localization has been studied by Köbler et al. [52]. Some advantages and disadvantages compared to non-local fatigue models have been discussed in Magino et al. [61]. In the context of non-localizing fatigue damage the damage model needs to be complemented by an appropriate criterion to predict failure. Moreover, the proposed model does not distinguish between tension and compression, but rather between loading and unloading. For similar models with tension-compression distinction, we refer to Ladevèze and co-workers [72,73].

3. The fatigue-damage model in cycle space

For high cycle fatigue experiments, the number of fatigue cycles is typically in the range of $10^3 - 10^6$ cycles. Thus, the computational cost of a numerical model resolving each individual cycle can be huge. In this section we first study the necessary time step resolution of the model introduced in section 2. We then reformulate the model in cycle space and logarithmic cycle space relying on approximations valid for the high cycle-regime for one Gaussian integration point. We demonstrate the capabilities of the model formulated in cycle space and logarithmic cycle space to use significantly larger steps. Subsequently, a combined time-scale and logarithmic cycle-scale approach is discussed that combines the accuracy of the time-scale model in the first few cycles with the computational efficiency of the logarithmic cycle space formulation at cycles exceeding 10^3 . Last but not least, we discuss the assumptions necessary to extend the reformulation obtained from one Gauss-Point to a full field computation and compare the damage evolution for time-scale and reformulated models on a generic fiber structure.

First, we study the necessary number of time (scale) increments for the model formulated in time scale (described by equations (2.5) and (2.7))

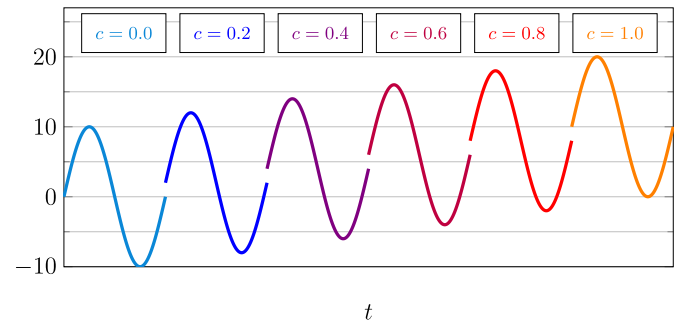


Fig. 3. Influence of shift parameter c on the wave form.

$$\dot{D}(\epsilon, D, q) = \begin{cases} \alpha_q(q) Y_D(\epsilon, D), & \text{if } \dot{Y}_D(\epsilon, D) \geq 0, \\ 0, & \text{otherwise,} \end{cases} \quad (3.1)$$

$$\dot{q} = K, \quad (3.2)$$

with the initial conditions $D(t = 0) = 0$ and $q(t = 0) = q_0$.

We use the same material parameters for the matrix material as for Fig. 1. We consider a sinusoidal uniaxial tension loading with a peak stress of $\sigma_{\max} = 60$ MPa and a stress ratio of $R = 0$. We discretize the evolution equation (3.1) with a backward Euler scheme, and select a reference time step for the time-scale model of $\Delta t = T/80$.

In Fig. 2, the evolution of the damage variable D under the described loading conditions for a pure matrix material is shown for different step sizes. We consider the relative error measure

$$e_{\text{step}}^x(N) = 2 \frac{\|D_x(N) - D_{\Delta/2}(N)\|}{\|D_x(N) + D_{\Delta/2}(N)\|} \quad (3.3)$$

to compare computations using different step sizes X to computations with the finest computed step $\Delta/2$. For $q_0 = 5.0$, the relative error for the time-scale model at $N = 10^3$ is $e_{\text{step}}^{\Delta} = 0.87\%$ for the reference time step and $e_{\text{step}}^{2\Delta} = 1.26\%$ for a time step twice the reference time step. The choice of a reference time step $\Delta t = T/80$ thus ensures the relative error to be below 1%. Thus, computing $N = 10^5$ cycles, a common cycle count for high-cycle fatigue, requires 8×10^6 time steps. This becomes prohibitive for complex microstructures or even heterogeneous materials.

We thus proceed by seeking a reformulation of the material equations in cycle and subsequently in logarithmic cycle space that allows for efficient computation at large cycle numbers. In experiments, the load path within one cycle is known a priori. We consider the most commonly used wave form in fatigue loading, the sinusoidal wave [74–78]. Knowing the wave form enables us to derive a model in cycle space from the time model discussed section 2 via integration. We assume a

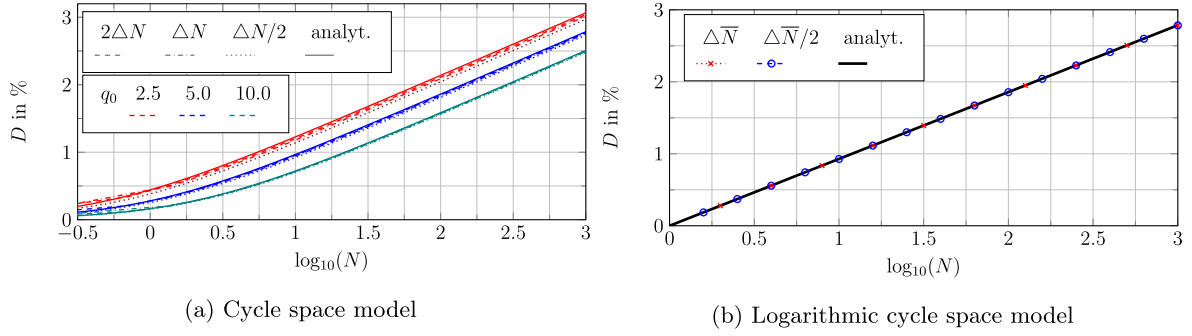


Fig. 4. Resolution study in terms of necessary (logarithmic) cycles.

sinusoidal wave form

$$\sigma = \left(\sin\left(\frac{2\pi}{T}t\right) + c \right) \sigma_a = (\sin(2\pi\tau) + c) \sigma_a \quad (3.4)$$

for a prescribed stress amplitude σ_a . As depicted in Fig. 3 for a load amplitude of $\sigma_a = 10$ MPa, the parameter c shifts the mean stress of the load path. The maximum stress during the cycle is defined at $\sigma_{\max} = \sigma_a(c + 1)$.

Plugging equation (3.4) into the damage evolution equation (2.5) yields

$$D(N+1) - D(N) = \int_0^1 \dot{D}(T(N+\tau)) d\tau = \begin{cases} \int_0^1 \frac{4\alpha_t}{q_0 + K(N+\tau)} Y_D d\tau, & \text{if } -(\sin(2\pi\tau) + c)\cos(2\pi\tau) \geq 0, \\ 0, & \text{otherwise.} \end{cases} \quad (3.5)$$

In the high cycle fatigue regime, the inequality $\tau \ll N + q_0/K$ holds. We thus use the approximation

$$q_0 + K(N+\tau) \approx q_0 + KN.$$

With these two approximations, we integrate the damage evolution under loading

$$D(N+1) - D(N) \approx \frac{2\alpha_t}{(q_0 + KN)} \sigma_a : \mathbb{S}_0 : \sigma_a \left(\int_{\frac{1}{4}}^{\frac{1}{2} + \frac{\arcsin(c)}{2\pi}} + \int_{\frac{3}{4}}^1 \right) (\sin(2\pi\tau) + c)^2 d\tau = \frac{\alpha_t}{q_0 + KN} \sigma_a : \mathbb{S}_0 : \sigma_a \left(\frac{1}{2} + c^2 \right). \quad (3.6)$$

Treating the cycle variable N as a continuous variable, we are led to the approximation

$$\frac{\partial D}{\partial N}(N) \approx \frac{\alpha_t}{q_0 + KN} \sigma_a : \mathbb{S}_0 : \sigma_a \left(\frac{1}{2} + c^2 \right).$$

Then, at constant stress amplitude σ_a and for an initial condition $D(N=0) = 0$, we may further integrate over the cycles to arrive at an explicit expression in cycle space

$$D(N) \approx \frac{\alpha_t}{K} \sigma_a : \mathbb{S}_0 : \sigma_a \left(\frac{1}{2} + c^2 \right) \log(KN + q_0). \quad (3.7)$$

At high cycle counts $N > 10^3$ and for typical values of $q_0 \in (0, 10]$ and $K \in [1, 10]$, the assumption $q_0 + KN \approx KN$ is valid. We thus may further approximate

$$D(N) \approx \frac{\alpha_t}{K} \sigma_a : \mathbb{S}_0 : \sigma_a \left(\frac{1}{2} + c^2 \right) (\log(N) + \log(K)). \quad (3.8)$$

For notational simplicity, we introduce the parameter

$\alpha = \alpha_t / (2K \log_{10}(e))$ and rewrite the damage evolution

$$D(N) \approx 2\alpha \sigma_a : \mathbb{S}_0 : \sigma_a \left(\frac{1}{2} + c^2 \right) (\log_{10}(N) + \log_{10}(K)). \quad (3.9)$$

We arrive at the final expression

$$D' = 2\alpha \sigma_a : \mathbb{S}_0 : \sigma_a \left(\frac{1}{2} + c^2 \right), \quad (3.10)$$

where we replaced the approximation by an equality sign and denote by prime the derivative w.r.t. the logarithmic cycle count $\bar{N} = \log_{10}N$, $D' \equiv \partial D / \partial \bar{N}$. Please note that cyclic loading for load waves different from the sinusoidal wave can be treated similarly. The sinusoidal wave form is just the most commonly used in fatigue experiments on short-fiber reinforced polymers.

We derived approximate models in different time-like scales. To sum up, we obtained.

1. an evolution equation in cycle space

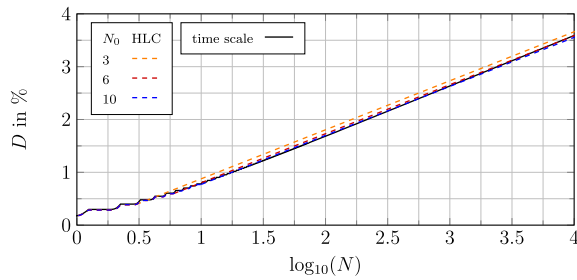
$$\frac{\partial D}{\partial N} = \frac{\alpha_t}{q_0 + KN} \sigma_a : \mathbb{S}_0 : \sigma_a \left(\frac{1}{2} + c^2 \right), \quad (3.11)$$

2. an evolution equation in logarithmic cycle space

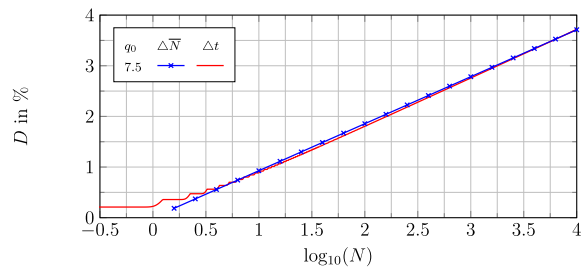
$$\frac{\partial D}{\partial \bar{N}} \equiv 2\alpha \sigma_a : \mathbb{S}_0 : \sigma_a \left(\frac{1}{2} + c^2 \right). \quad (3.12)$$

We study the necessary resolution in cycle space for the models at hand. We discretize the above equations using a backward Euler scheme and use reference step sizes of $\Delta N = 1/8$ for the cycle model and increase the step size for the logarithmic model according to the relation $\Delta N = 2N$ dependent on the current cycle N . In Fig. 4, the evolution of the damage variable D is shown for pure tension loading with a stress ratio $R = 0$ and a stress amplitude of $\sigma_a = 30$ MPa. In Fig. 4(a), we observe that the influence of the parameter q_0 is restricted to the first few cycles of the damage evolution. Indeed, after ten or more cycles ($\log_{10} > 1$), the slope of the damage evolution is almost independent of q_0 . In Fig. 4(b), the damage evolution computed in logarithmic cycle space is shown. By the assumption $q_0 + KN \approx KN$, used in the derivation of the logarithmic model, the influence of a varying initial value of q_0 is neglected in the model formulated in logarithmic cycle space. Thus, the material evolution in the logarithmic cycle-scale model is independent of q_0 .

We use the error measure (3.3) to quantify the deviations of the numerical computations depending on the resolution. At the cycle count $N = 10^3$, the relative error for the cycle space model with $q_0 = 5.0$ is $e_{\text{step}}^{\Delta} = 0.44\%$ and $e_{\text{step}}^{2\Delta} = 1.30\%$ for the reference and a time step twice the reference step, respectively. Thus, using the reference cycle step with $\Delta N = T/8$, the relative error is below 1%. When using the logarithmic cycle model, the reference time step $\Delta \bar{N} = 0.3 \log_{10}N$ is not constant in



(a) HLC-approach using different numbers of cycles N_0 for initial time-scale based computation for $q_0 = 10.0$



(b) Damage for the time-scale model with $q_0 = 7.5$ and the logarithmic cycle-scale model with $D(\bar{N} = 0) = 0$

Fig. 5. Comparison of the damage evolution predicted by the time-scale, the HLC and the logarithmic cycle-scale approach.

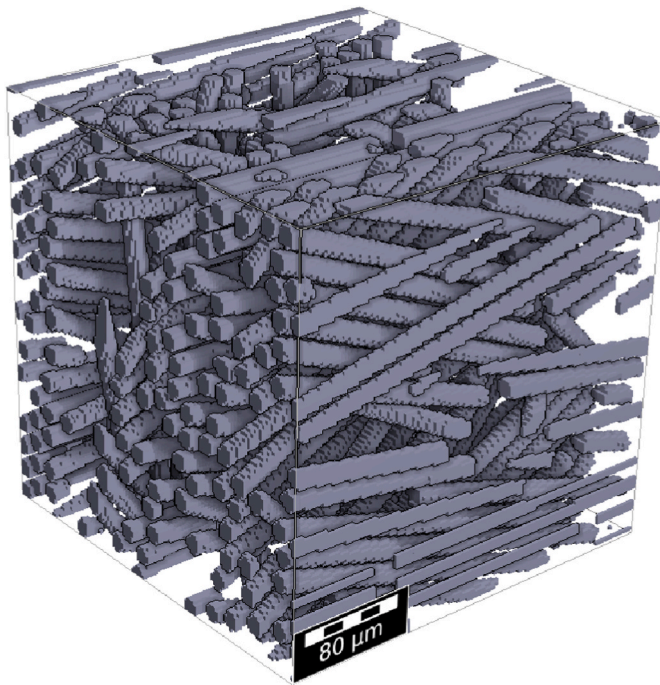


Fig. 6. Generic structure.

cycle space. Thus the gain in computational efficiency depends on the computed number of cycles. For high-cycle fatigue with a typical cycle number of $N = 10^5$, or $\bar{N} = 5$, respectively, the necessary number of cycle steps is $N_{\Delta N}^{\text{necess}} = 8 \times 10^5$. The number of necessary steps in logarithmic cycle space is 17. This is a speed-up by a factor of 4.7×10^5 or 4.7×10^4 in comparison with the cycle-scale model and the time-scale model, respectively.

Even though the reformulation of the material model in logarithmic cycle scale comes with a significant computational speed up, the approximations made in the derivation of the evolution equations do not account for the material evolution in the first few cycles of the material under fatigue loading. As a remedy, consider an approach which combines the accuracy of the time-scale model with the computational efficiency of the model in logarithmic cycle space. In this combined approach, to which we will refer as Hybrid Log-Cycle model (HLC) in the following, the first few cycles N_0 are computed explicitly in time scale. The damage field at the last cycle computed in time scale is then used as the initial condition for the logarithmic cycle-scale model. Hence, the rapidly changing damage evolution behavior in the initial phase can be accounted for, while the computational efficiency remains reasonable at large cycles.

In Fig. 5(a), the HLC-approach is investigated for different cycle

Table 1

Geometric properties of the generic fiber structure.

Property	value	unit
Second order fiber-orientation tensor	$\begin{bmatrix} 0.77 & 0 & 0 \\ 0 & 0.21 & 0 \\ 0 & 0 & 0.02 \end{bmatrix}$	–
Fiber length	300	μm
Fiber diameter	13	μm
Voxel length	2.5	μm
Fiber-volume content	17.8	%
Size	128^3	–

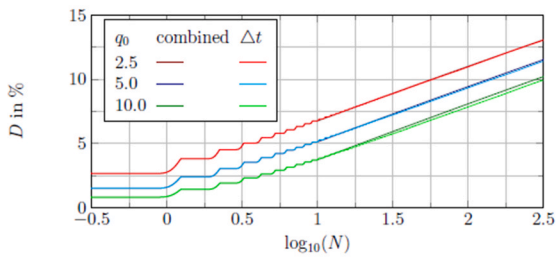
numbers computed in time scale N_0 . Here, the parameter $q_0 = 10$ is chosen. For reference, the corresponding damage evolution computed in time scale is plotted in black. We observe that, for increasing number of computed cycles in time space N_0 , the deviation between the HLC and the time-scale evolution becomes smaller. Indeed, while, for $N_0 = 3$ and $N_0 = 6$, the deviations between the two approaches are still noticeably large, the deviation between HLC and time-scale model for $N_0 = 10$ is barely visible. For $N_0 = 10$, the deviations between the curves are reasonably small, i.e., the relative deviation at $N = 10^3$ is 0.46%.

Arguing in the opposite direction is also possible, i.e., we asked ourselves the question whether there are suitable material parameters, such that the model parametrized in time and the log-cycle model with $D(\bar{N} = 0) = 0$ are reasonably close. This can indeed be done, but involves some tinkering. For $q_0 = 6.5$, a suitable agreement can be reached, see Fig. 5(b). More precisely, we observe that the damage evolution of the two models is similar for cycles larger than 100. Indeed, the relative deviation of the damage value for both models at $\bar{N} = 2.5$ is 1.17%.

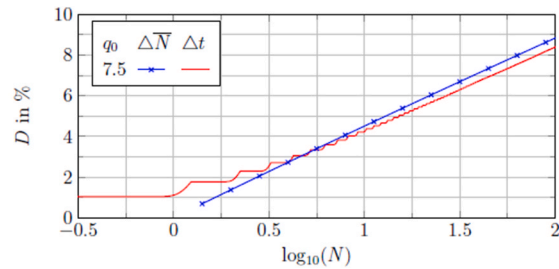
Last but not least, we study the model embedded in a multiscale framework, i.e., the effective strains emerging from a composite material with linear elastic fibers and a matrix material governed by the novel fatigue-damage model. Considering a microstructure shown in Fig. 6, we assume that the stress field does not largely deteriorate during one loading cycle, i.e., that the change in the damage field during one cycle is small. If the structure is subjected to proportional loading within one cycle, i.e. $\sigma_a(x, t) = \bar{\sigma}_a(N, x)\bar{\sigma}_a(\tau)$, the derivation of the Gauss-point equations can be extended to full field equations.

To study the emerging fields numerically, we make use of a "generic" fiber structure. The geometric properties of the microstructure are listed in Table 1. The structure is subjected to load-driven uniaxial sinusoidal tension with an amplitude of 60 MPa and a stress ratio of $R = 0$. Similar to the pure matrix material, we compare the HLC and the time-scale computations for the generic structure in Fig. 7(a). Here, we chose $N_0 = 10$ for the HLC model. In Fig. 7(a), the maximum of the current damage field in the structure is plotted. The resulting deviation at $\bar{N} = 2.5$ is 0.28%, 0.96% and 2.62% for chosen $q_0 = 2.5$, $q_0 = 15.0$ and $q_0 = 10.0$, respectively.

In Fig. 7(b), we compare the evolution of the current maximum of the damage field in the generic structure for the time-scale model with



(a) Damage evolution for HLC-approach using $N_0 = 10$ at different values of q_0 vs. time-scale approach on generic structure



(b) Damage for the time-scale model with $q_0 = 7.5$ and the logarithmic cycle-scale model with $D(\bar{N} = 0) = 0$ for the generic structure

Fig. 7. Comparison of the damage evolution using time-scale, HLC and logarithmic cycle-scale approach for the generic structure.

$q_0 = 6.5$ to the logarithmic cycle-scale model with the initial condition $D(\bar{N} = 0) = 0$. Analogously to the computations on the pure matrix material, the deviation of the evolution damage is small, i.e., 1.55% at $\bar{N} = 2.5$.

To sum up, the formulation in logarithmic cycle space offers an extremely efficient way to compute the stiffness loss of a material subjected to stress ratios between -1 and 0 . The N_0 -dependent stiffness loss in the first few cycles can be accounted for by a combined time-cycle scale approach. For the remainder of the manuscript we chose to use $q_0 = 6.5$ instead, which corresponds to an initial condition $D(\bar{N} = 0) = 0$ as confirmed in the above numerical experiments. The load amplitude σ_a and maximum stress σ_{max} enter the evolution equation via an effective stress

$$\sigma_{eff} = \sigma_a \sqrt{1 + 2c^2}, \quad (3.13)$$

where c is implicitly defined via $\sigma_{max} = (1 + c)\sigma_a$.

We conclude this section with a few remarks.

For a start, the fatigue-damage model formulated in logarithmic cycle space resembles the model proposed in Magino et al. [61], using the effective stress (3.13) instead of the maximum stress σ_{max} . In this work [61], the authors did not concern themselves with time-upscaling techniques but directly formulated the material model in the logarithmic time domain, motivated by experimental results shown in section 5.

With the time-scale formulation and the upscaling approach at hand, we are able to extend the model to different R-values in a straightforward and consistent manner.

Moreover, the model formulated in logarithmic cycle space, as discussed more thoroughly in Magino et al. [61], can be viewed as generalized standard material (GSM) [79,80]. This perspective enables to recast the model in terms of an optimization problem.

4. Efficient computation of fiber-reinforced components

We are interested in the effective behavior of short-fiber reinforced composites. Consider a cubic cell $Y \subseteq \mathbb{R}^3$, on which a heterogeneous field of compliance tensors $Y \ni x \mapsto \mathbb{S}_0(x)$ and a characteristic function $\xi: Y \rightarrow \{0, 1\}$ are given. The latter describes the material distribution at every point $x \in Y$, i.e., $\xi^{-1}(1)$ is the domain of the matrix material and $\xi^{-1}(0)$ the domain of the fiber material.

We seek a displacement fluctuation field $u(x)$, a strain field $\epsilon(x)$, a stress field $\sigma(x)$ and a damage field $D(x)$ solving the balance of linear momentum

$$\text{div } \sigma(\bar{N}) = 0, \quad (4.1)$$

where we suppress the dependence on x , the kinematic compatibility condition

$$\epsilon(\bar{N}) = \langle \epsilon(\bar{N}) \rangle_Y + \mathbf{grad}^* u(\bar{N}), \quad (4.2)$$

the constitutive equation formulated in a stress-explicit manner

$$\epsilon(\bar{N}) = \xi(1 + D(\bar{N})) \mathbb{S}_0 : \sigma(\bar{N}) + (1 - \xi) \mathbb{S}_0 : \sigma(\bar{N}) \quad (4.3)$$

and the evolution of the internal variable $D(\bar{N})$

$$D' = \frac{\alpha}{2} \sigma(\bar{N}) : \mathbb{S}_0 : \sigma(\bar{N}), \quad (4.4)$$

prescribing an effective stress $\Sigma_{eff}(\bar{N})$

$$\langle \sigma \rangle_Y(\bar{N}) = \Sigma_{eff}(\bar{N}) = \sqrt{\frac{1}{2} + c^2} \Sigma_a(\bar{N}), \quad (4.5)$$

where $\langle \cdot \rangle_Y$ stands for averaging over the cell Y . Σ_a refers to the stress amplitude tensor. Discretizing the time-like variable \bar{N} recovers the (mixed) variational principle of Magino et al. [61]

$$S(\sigma, D) \rightarrow \min_{D \geq 0} \max_{\langle \sigma \rangle_Y = \Sigma_{eff}} \text{div } \sigma = 0, \quad (4.6)$$

where we replaced the prescribed stress amplitude Σ in the previous formulation by the effective stress Σ_{eff} in terms of the saddle-point function

$$S(\sigma, D) = \langle -\xi \frac{(1+D)}{2} \sigma : \mathbb{S}_0 : \sigma + \xi \frac{1}{2\alpha \Delta \bar{N}} (D - D^n)^2 + (1 - \xi) \frac{1}{2} \sigma : \mathbb{S}_0 : \sigma \rangle_Y \quad (4.7)$$

with $D^n = D(\bar{N}^n)$ at the previous time increment.

To compute the effective behavior of the material on component scale, we follow the model-order reduction strategy proposed in of Magino et al. [61]. Indeed, to use the framework for arbitrary R-values, we only need to adjust the macroscopic effective stress Σ_{eff} according to equation (3.10). In other words, a material database trained with a certain load amplitude and R-value can be used to compute the material behavior for different amplitudes and stress ratios by applying a modified effective stress to the material on the macroscale. As discussed in section 3, in some cases, like an arbitrary choice of N_0 , the user might be interested in a combined time-cycle-scale approach. As stated in section 3, for the manuscript at hand, we will stick to the logarithmic cycle-scale model with $q_0 = 7.5$.

5. Comparison to experimental data

We demonstrate the capability of the model to reproduce the stiffness degradation in short-fiber reinforced components by comparing the model predictions to experimental data of reinforced PA polyamide 6.6.

First, we discuss the material characterization process and the experimental setup. Subsequently, we discuss the numerical material-characterization procedure. Finally, we compare numerical predictions

Table 2
Mechanical properties of the constituents.

Property	Matrix	Fiber
Young's modulus	3.35 GPa	72.0 GPa
Poisson's ratio	0.38	0.22
Damage parameter α	0.1 1/MPa	-

and experimental results for the proposed model at different load scenarios, stress ratios and fiber orientations.

5.1. Experimental setup and parameter identification

Fatigue experiments for specimens with different fiber orientations, geometries, load amplitudes and stress ratios were performed.

The material is a commercial polyamide 6.6 reinforced by 35 wt% short E-glass fibers. The material properties of the constituents are listed in Table 2.

The specimens were milled from an injection-molded plate with dimensions $80 \times 80 \times 2 \text{ mm}^3$. For more details about the injection-molding process, we refer to Hessman et al. [81], Fig. 1]. Depending on the orientation of the specimen length w.r.t. the injection direction of the thermoplastic material, we refer to the specimens as 0° -oriented and 90° -oriented [81]. Due to the injection-molding process, the specimens show a characteristic fiber structure forming layers of different local fiber orientations. To obtain the fiber-orientation distribution over the depth of the specimen, a control volume was cut from the center of the plate. Subsequently, the volume was characterized via X-ray micro-computed tomography (μ CT) and the fiber-segmentation algorithm introduced by Hessman et al. [82].

We performed fatigue experiments on three different specimen geometries, shown in Fig. 8. The different geometries differ by the radius of the notch. The first specimen is devoid of notches. We refer to it as specimen A in the further discussion. Specimen B is a mildly notched specimen with a notch radius of 2 mm. The third geometry with a notch

radius of 0.05 mm is the most sharply notched considered for the presented experiments. We refer to it as specimen C.

The specimens were subjected to sinusoidal stress-driven loadings at different amplitudes σ_a for the stress ratios $R = 0$ and $R = -1$. For stress ratios of $R = -1$, a buckling column was employed to avoid buckling of the specimens during fatigue testing. The strains were measured at the surface of the fatigue specimens, with an extensometer of a reference length $l_0 = 20 \text{ mm}$ for all experiments with stress ratios values of $R = 0$ and an extensometer of a reference length $l_0 = 5 \text{ mm}$ for all experiments with stress-ratio values of $R = -1$. The frequencies in the experiments ranged between 0.5 and 5 Hz and were selected to ensure that the temperature changes at the specimen surfaces remain below 2 K.

We are interested in the loss of the dynamic stiffness of the material under fatigue loading. Thus, we recorded the maximum strain ϵ_{\max} and the minimum strain ϵ_{\min} for every (reported) cycle. The dynamic stiffness of the specimen is then calculated by

$$E_{\text{dyn}} = \frac{\sigma_{\max} - \sigma_{\min}}{\epsilon_{\max} - \epsilon_{\min}} \tag{5.1}$$

The evolution of the dynamic Young's modulus for specimens oriented in 0° - as well as 90° -direction and for stress ratios of $R = 0$ is shown in Fig. 9. The experiments were conducted at different stress amplitudes σ_a . We observe that the dynamic stiffness of the specimen decreases over the load history. The higher the load amplitude applied to the specimen, the faster is the degradation process. They show a stable regime of stiffness degradation up to 10^3 - 10^6 cycles depending on the loading amplitude. Subsequent to this stable regime, the specimens enter a regime of unstable failure. This regime is characterized by massive fluctuations in the measured specimen as the strain extensometer may be distorted and a steep decent in the stiffness. To gain a more thorough understanding of the available data, a linear function of the form

$$E_{\text{dyn}}(\bar{N}) = E_{\text{dyn}}^0 - k\bar{N} \tag{5.2}$$

is used to model the data, where E_{dyn}^0 represents the initial dynamic

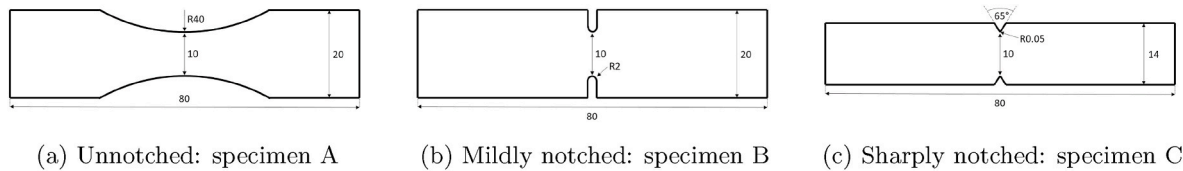


Fig. 8. Test geometries subjected to cyclic loading.

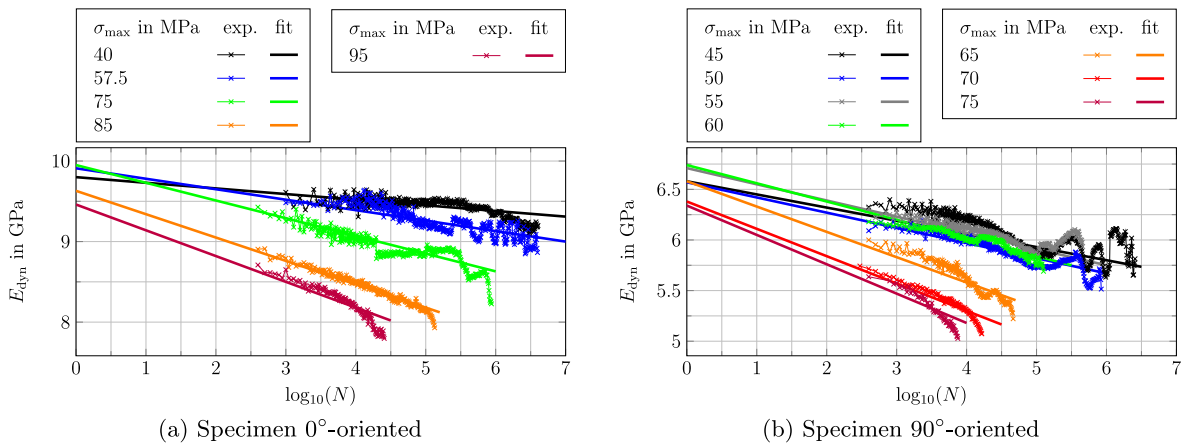


Fig. 9. Evolution of the dynamic Young's modulus E_{dyn} for specimen A and $R = 0$, fitted to the model function $E_{\text{dyn}}(\bar{N}) = E_{\text{dyn}}^0 - k\bar{N}$

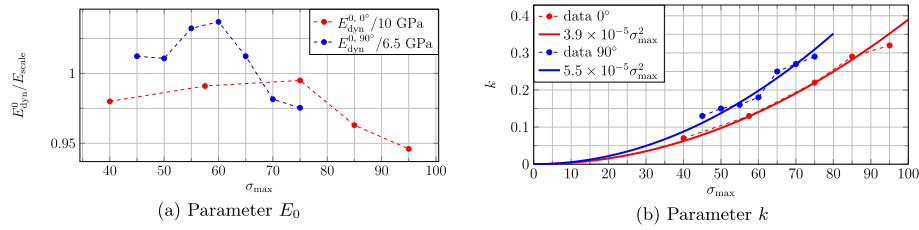


Fig. 10. Parameters obtained by fitting to the model function (5.2).

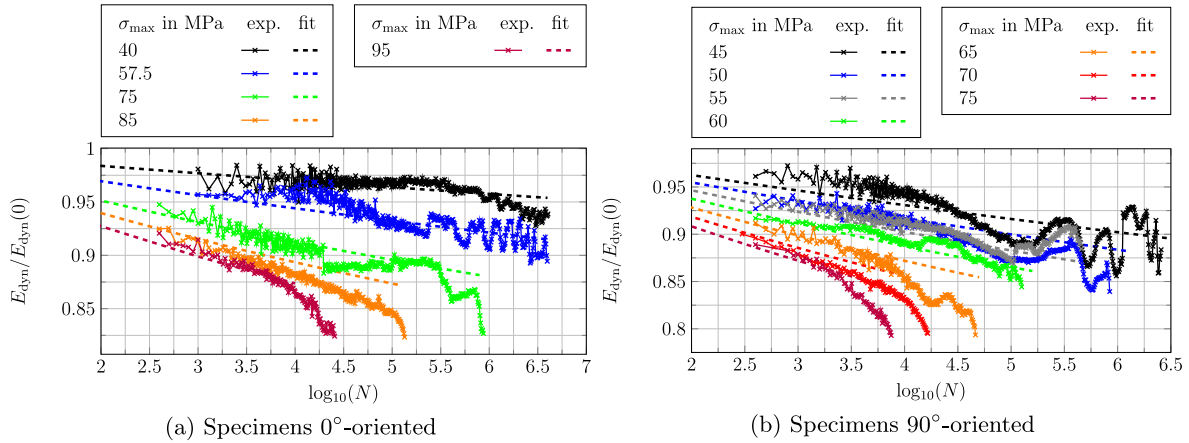


Fig. 11. Parameter identification for fatigue-damage model predictions using experimental data for $R = 0$ and specimen A with parameter $\alpha = 0.1$ 1/MPa.

Young’s modulus of the specimen at $\bar{N} = 0$ and the parameter k characterizes the speed of the stiffness degradation. For each individual stiffness evolution curve, the parameters of the model function (5.2) were identified via linear regression. The resulting fits are displayed in Fig. 9. We observe a profound scattering of the initial Young’s modulus E_{dyn}^0 . For measurements on 90°-oriented specimens, this effect is even more pronounced than for the measurements of the 0°-oriented specimens, and is of the order of 5%.

The parameters k and E_{dyn}^0 are plotted in Fig. 10. The initial stiffness E_{dyn}^0 for 0°-oriented specimens scatters between 9.95 MPa and 9.46 MPa, which is a relative deviation of 5.2%. For the 90°-oriented specimens, the values of E_{dyn}^0 lie between 6.74 MPa and 6.34 MPa, which is a relative deviation of 6.3%. The initial stiffness E_0 seems to decrease with the applied loading amplitude. There are several reasons for this rather surprising behavior. First, thermoplastics are well-known to be viscoelastic in nature. The experiments at different stress amplitudes are also performed at different frequencies. This is due to an optimization between time expense of the experiment and a restriction of the self-heating of the material. Thus higher amplitudes are driven with lower frequencies and their measured dynamic modulus appears to be higher. Another possible explanation is fiber breakage during the first loading cycle. However, the stiffness decrease, represented by the parameter k , seems to be fairly reproducible. Indeed, plotting k over the stress

maximum σ_{max} for the 0°-specimens and 90°-oriented specimens in Fig. 10(b), k roughly follows a quadratic trend.

We conclude that there is a significant statistical scattering in the dynamic stiffness. This might be due to the underlying random microstructure obtained from the injection modeling. In particular the initial dynamic stiffness of the specimens shows significant variation. However, when focusing on the relative stiffness degradation, the decrease under fatigue-loading seems to be quite reproducible. In the work at hand, we do not concern ourselves with the modeling of statistical fluctuations of the initial specimen stiffness. Rather, we focus on the fatigue-damage effects on the material. We thus normalize all experimental data with the use of the model function (5.2) and use the obtained data as our point of departure for fatigue-damage modeling.

To identify the material parameter α of the fatigue-damage model, the relative dynamic Young’s modulus decrease of specimen An under loading with a stress ratio of $R = 0$ is used.

As shown in Köbler et al. [52] for a similar material model, the parameter α governing the damage evolution speed can be regarded as rescaling of the time scale

$$\frac{dD}{d(\rho\bar{N})} = 2 \frac{\alpha}{\rho} \sigma_a : \mathbb{S}_0 : \sigma_a \left(\frac{1}{2} + c^2 \right). \quad (5.3)$$

For the identification of the material parameter α it is thus possible to compute a load case and adjust the damage evolution speed afterwards by rescaling the (pseudo) time \bar{N} . The results for an identified material parameter of $\alpha = 0.1$ 1/MPa are shown in Fig. 11. Note that only a single parameter for the matrix material is identified. Then, the material behavior of the composite material is fully identified.

The computed results for the composite material with different orientation states 0° and 90° show a good agreement with the experimental results. At different load amplitudes and material orientations, the degradation of the material in the steady fatigue-damage regime prior to failure can be reproduced.

Table 3
Properties of the generated microstructures.

Property	Value	Unit
Fiber length [88]	300	μm
Fiber diameter [88]	13	μm
Fiber aspect-ratio	23	–
Fiber-volume content	19.5	%
Minimum fiber distance	5	μm
Voxels per diameter	6.4	–
Cell length/Fiber length	2.6	–

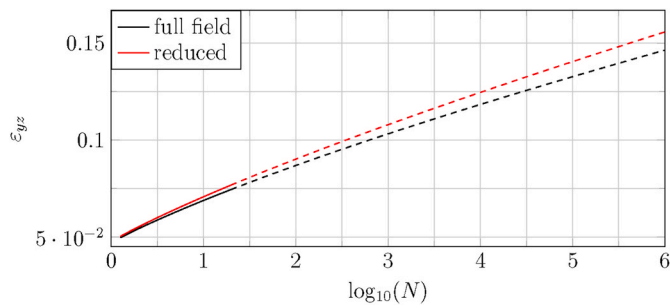


Fig. 12. Evolution of ϵ_{yz} in fiber structure with $\lambda_1 = 0.903$, $\lambda_2 = 0.069$ with $N < N_{\text{step}}$ (solid) and $N > N_{\text{step}}$ (dashed).

5.2. Numerical characterization of the material

To characterize the behavior of the short-fiber reinforced material we rely on computational homogenization. As discussed in section 4, we treat the matrix as a material undergoing damage. The short E-glass fibers are treated as an isotropic, purely elastic material.

With the fiber-orientation interpolation method [83] in mind, we solve the microscale problem discussed in section 4 using an FFT-based solution algorithm implemented in the software FeelMath [84] on a number of microstructures. The fiber structures are generated using the sequential addition and migration algorithm (SAM) [85] using the properties and spatial discretization listed in Table 3. We use the staggered grid discretization [86] in space and a nonlinear conjugate gradient method to reduce the strain residual suggested by Kabel et al. [87] below a tolerance of 10^{-5} . The framework of fiber-orientation interpolation [83] allows the engineer to fully characterize the material behavior of short-fiber reinforced composites with arbitrary fiber orientations using only a *finite* number of precomputations on the microstructures. The basic steps are the following.

1. Discretization of the space of possible fiber orientations $\{\mathcal{O}_i\}$.
2. Generation of fully-resolved fiber structures $\{Y_i\}$ for ever fiber-orientation $\{\mathcal{O}_i\}$.
3. Discretization of the space of possible load paths $\{\Sigma_{\text{eff},j}\}$.
4. Precomputation of the material degradation on the fiber structures $\{Y_i\}$ under the load paths $\{\Sigma_{\text{eff},j}\}$.
5. POD-analysis of the strain field paths for every structure Y_i and identification of system matrices for the reduced model for the fiber orientation \mathcal{O}_i .

The material behavior of an *arbitrary* microstructure characterized

by its second-order fiber-orientation tensor [89] is then interpolated from three fiber orientations included in the set of precomputed structures which are closest to the unknown fiber-orientation state. For details we refer to Köbler et al. [83].

For this work, characterizing the PA6.6 material used in the experiments, we used the following parameters:

1. Equidistant triangulation of the fiber-orientation triangle with 15 fiber-orientation nodes as shown in Fig. 13(a).
2. Generation of the microstructures using the parameters given in Table 3.
3. Choice of six load cases: three pure extension (in x -, y - and z -direction, respectively) and three shear load cases (in the xy -, xz - and yz -planes, respectively) with a constant effective stress amplitude $\Sigma_{\text{eff}}(\bar{N}) = 100$ MPa for $\bar{N} \in [0, 6]$.
4. Precomputation of the material degradation on the microstructures for the respective six load paths.
5. POD-analysis with ten snapshots per load path.

To quantify the accuracy of the used model-order reduction and interpolation strategy, we define a strain error measure

$$e^{\text{rom}} = \max_{N_i \in [0, N_{\text{steps}}]} \frac{\|\bar{\epsilon}_{\text{eff}}(\bar{N}_i) - \bar{\epsilon}_{\text{eff}}^{\text{rom}}(\bar{N}_i)\|}{\|\bar{\epsilon}_{\text{eff}}(\bar{N}_i)\|}, \quad (5.4)$$

where the number N_{steps} of considered load steps to compute the error is implicitly defined by

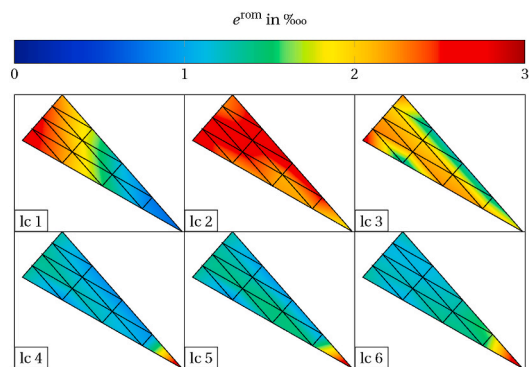
$$\|\bar{\epsilon}_{\text{eff}}(N_{\text{steps}})\| = 1.5 \|\bar{\epsilon}_{\text{eff}}(0)\|. \quad (5.5)$$

here, $\bar{\epsilon}_{\text{eff}}$ denotes the effective strain of the full-field solution and $\bar{\epsilon}_{\text{eff}}^{\text{rom}}$ refers to the effective strain of the reduced order model. The choice of

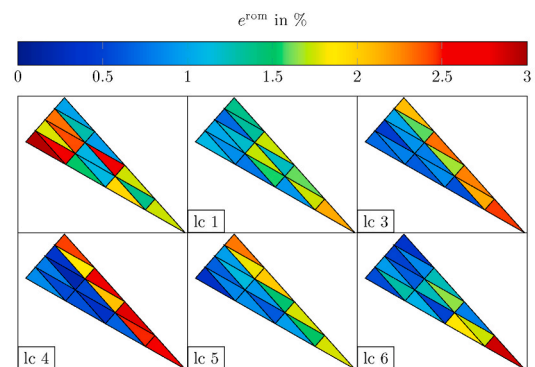
Table 4

Tensor components of the effective stress for precomputed load cases used in the database generation with training amplitude $\sigma^{\text{II}} = 100$ MPa.

load case	Σ_{xx}^{eff}	Σ_{yy}^{eff}	Σ_{zz}^{eff}	Σ_{xy}^{eff}	Σ_{xz}^{eff}	Σ_{yz}^{max}
# 1	σ^{II}	0	0	0	0	0
# 2	0	σ^{II}	0	0	0	0
# 3	0	0	σ^{II}	0	0	0
# 4	0	0	0	σ^{II}	0	0
# 5	0	0	0	0	σ^{II}	0
# 6	0	0	0	0	0	σ^{II}



(a) Strain error (5.4) at precomputed microstructures



(b) Strain error (5.4) at interpolated microstructures

Fig. 13. Accuracy of model-order reduction and fiber interpolation for the considered load cases (lc).

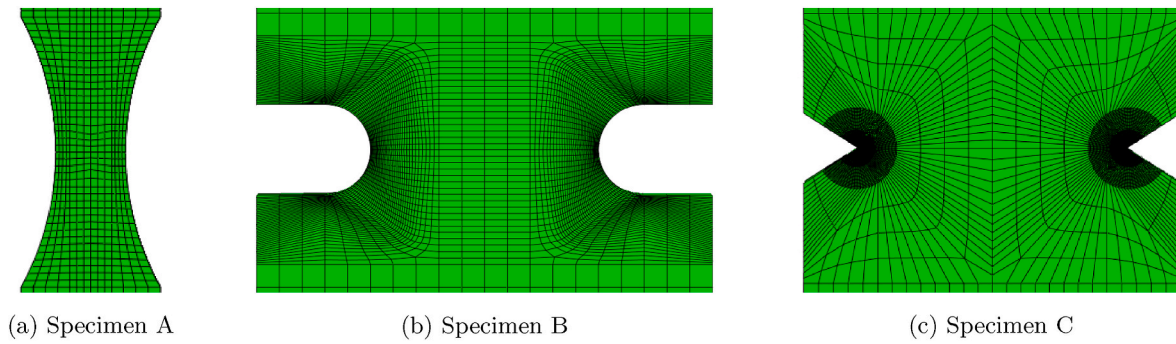


Fig. 14. Reference discretization h .

this strain measure is motivated by the observation that the full field and the reduced order solution increasingly differ with increased cycle number, or damage respectively. In Fig. 12 the strain evolution of the full field solution for a fiber orientation tensor with eigenvalues $\lambda_1 = 0.903$, $\lambda_2 = 0.069$ to its model order reduced (interpolated) evolution is shown. This case will be identified as the most critical one in terms of approximation in Fig. 13(b). The cycle at which the strain error is computed strongly influences the error magnitude. As fatigue experiments show that a stiffness decrease prior to fracture is in the order of a few ten percent, we consider the choice of (5.5), which roughly corresponds to a stiffness decrease of 33.3%, to be sufficient.

We consider the load cases listed and labeled in Table 4. In the following, we use the error measure to quantify the errors introduced by the model-order reduction and by the fiber-orientation interpolation for these load cases.

First, we study the error introduced by the model-order reduction approach. In Fig. 13(a), the strain error measure is shown for every microstructure included in the training set (15 points of the fiber orientation triangle) and every training load case (1c) 1–6. For each of them, the strain error measure (5.4) is plotted for the reduced order model incorporating 15 strain and 15 damage modes. The error is well below 0.1% for all structures and load cases studied.

Secondly, we compare the predictions of the reduced order model interpolated to the centroids of the fiber orientation triangle to the full-field solution on microstructures directly generated and computed for the orientations at the elements' centroids. The arising error is a sum of errors due to the randomness of the statistical volume element, the model-order reduction and the interpolation approach. The error remains below 3% for all studied structures and load cases and is thus considered to be acceptable for the remainder of the manuscript.

5.3. Comparison of numerical predictions to experimental data

To compute the fatigue damage in the specimens A-C (see Fig. 8), we use a finite element discretization with isoparametric, trilinear eight-

node brick elements in space and an implicit Euler scheme for time integration. The layered fiber-orientation distribution in the specimens obtained from a μ CT-scan analysis is used to determine the fiber-orientation distribution over the thickness of the specimens. We use a resolution of nine elements in thickness direction and assign an individual fiber-orientation according to the measurements to each of these layers.

The computations on the macroscale were performed with the commercial finite element software Abaqus [90].

To ensure accurate computations, we study the dependence of two computed properties on the mesh spacing.

The specimen stiffness $E_{\text{spec}}(\bar{N})$ is computed as a function of the logarithmic cycle scale \bar{N} . Here, the contact points of the strain gauge u_0 and u_1 with a reference length of l_0 in the experiments were chosen as measurement points for the displacement which determines the specimen stiffness

$$E_{\text{spec}} = l_0 \frac{F}{A_{\text{undef}}(u_0 - u_1)}, \quad (5.6)$$

where F is the extensional force and A_{undef} is the cross-sectional area of the undeformed specimen. Secondly, we define a fatigue-damage indicator Λ , which is a local quantity, depending implicitly on the geometry of the notch under consideration. This quantity is computed from the determinant of the acoustic tensor A^{aco} [89] via

$$\Lambda(\bar{N}) = \max_{\|\mathbf{n}\|=1} \left[1 - \frac{\det A^{\text{aco}}(\mathbf{n}, \mathbb{C}(\bar{N}))}{\det A^{\text{aco}}(\mathbf{n}, \mathbb{C}(0))} \right]. \quad (5.7)$$

We evaluate the fatigue-damage indicator $\Lambda(\bar{N})$ at the point of maximum damage and plot and study the evolution of this local property.

The reference meshes and the refined meshes of the three geometries are shown in Fig. 14 and Fig. 15, respectively. Notice, that the resulting element sizes in both meshes at the notch are smaller than the RVE. We chose the element size to accurately resolve the stress gradient. Thus,

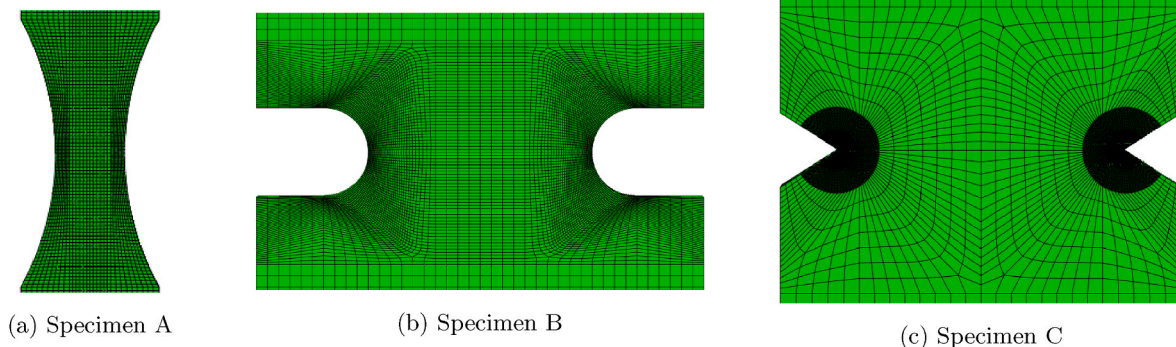


Fig. 15. Refined discretization $h/2$.

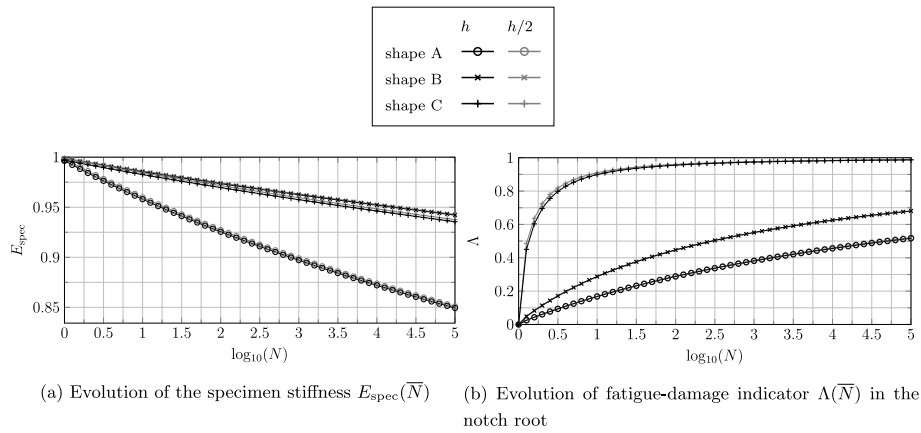


Fig. 16. Resolution study for different specimens.

Table 5

Relative errors of the resolution study at $\bar{N} = 5$

Specimen	error in stiffness	error in Λ
A	0.19%	0.73%
B	0.09%	0.39%
C	0.27%	0.17%

scale separation is presumably violated and the averaged stiffness of the computed composite material may not be applicable. In fact, the exact position and orientation of a *single* fiber close to notch may influence the damage evolution of the specimen greatly. The model at hand can not account for these effects. However, we chose the element size to resolve the stress gradient at the notch.

Both, the specimen stiffness E_{spec} and the fatigue-damage indicator Λ in the notch root, are compared for both meshes in Fig. 16. In the considered load cases, the location of maximal damaged point is not moving. Thus, the location at which the fatigue damage indicator Λ is plotted remains constant throughout the cycle evolution in Fig. 16(b). Note that under different loading conditions the point of maximum damage must not necessarily remain at the same location due to stress redistribution. The specimens A, B, and C were subjected to an effective stress $\sigma_{\text{eff}} = F/A_{\text{undef}} = 82.3$ MPa, $\sigma_{\text{eff}} = 65.0$ MPa and $\sigma_{\text{eff}} = 52.0$ MPa, respectively. For all three specimens and both the integral quantity E_{spec} and the local field quantity Λ , the deviations due to the different meshes are rather small. More specifically, using the relative error measures

$$e_{\text{rel}}^E(\bar{N}) = 2 \frac{\left\| E_{\text{spec}}^h - E_{\text{spec}}^{h/2} \right\|}{\left\| E_{\text{spec}}^h + E_{\text{spec}}^{h/2} \right\|}, \quad (5.8)$$

$$e_{\text{rel}}^\Lambda(\bar{N}) = 2 \frac{\left\| \Lambda^h - \Lambda^{h/2} \right\|}{\left\| \Lambda^h + \Lambda^{h/2} \right\|}, \quad (5.9)$$

the deviations at $\bar{N} = 5$ for the specimen stiffness E_{spec} and the fatigue-damage indicator Λ in the notch root are given in Table 5. All of the relative errors are well below 1%. Thus, the coarser mesh of the two is fixed for the remainder of the script.

To gain a deeper understanding of the emerging damage fields, the fatigue indicator Λ is plotted in Fig. 17. We consider the 0° -oriented specimens subjected to effective stresses $\sigma_{\text{eff}} = 82.3$ MPa, $\sigma_{\text{eff}} = 65.0$ MPa and $\sigma_{\text{eff}} = 52.0$ MPa for specimen A, B and C, respectively, at $\bar{N} = 5$.

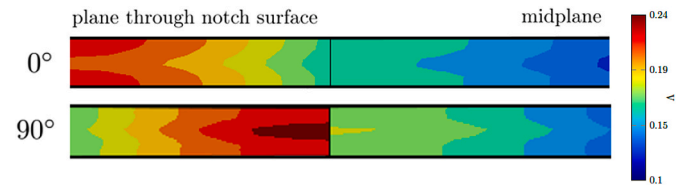


Fig. 18. Fatigue-damage over specimen depth: for 0° - and 90° -oriented specimen A in planes parallel to loading direction: through notch surface (right) and specimen center (left).

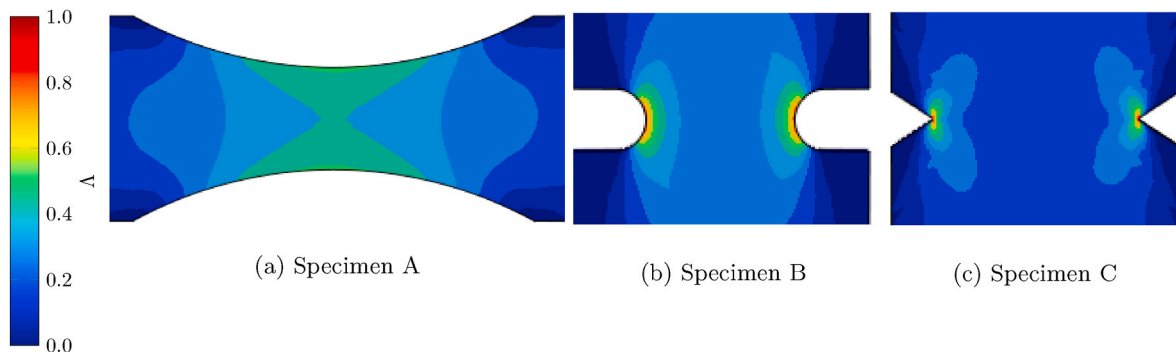


Fig. 17. Fatigue-damage indicator Λ at the surface of specimens at $\bar{N} = 5$

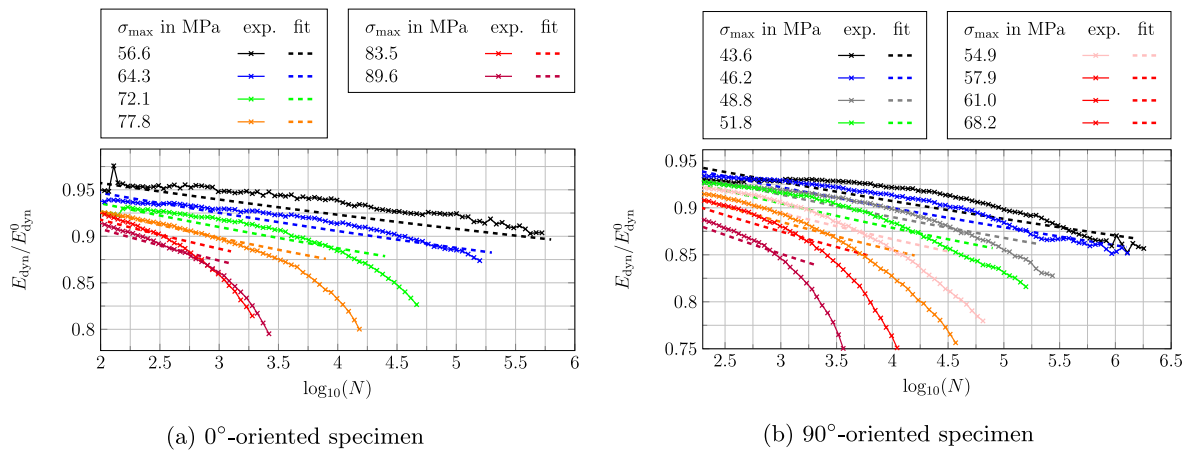


Fig. 19. Comparison of computational and experimental results for $R = -1$ and specimen A.

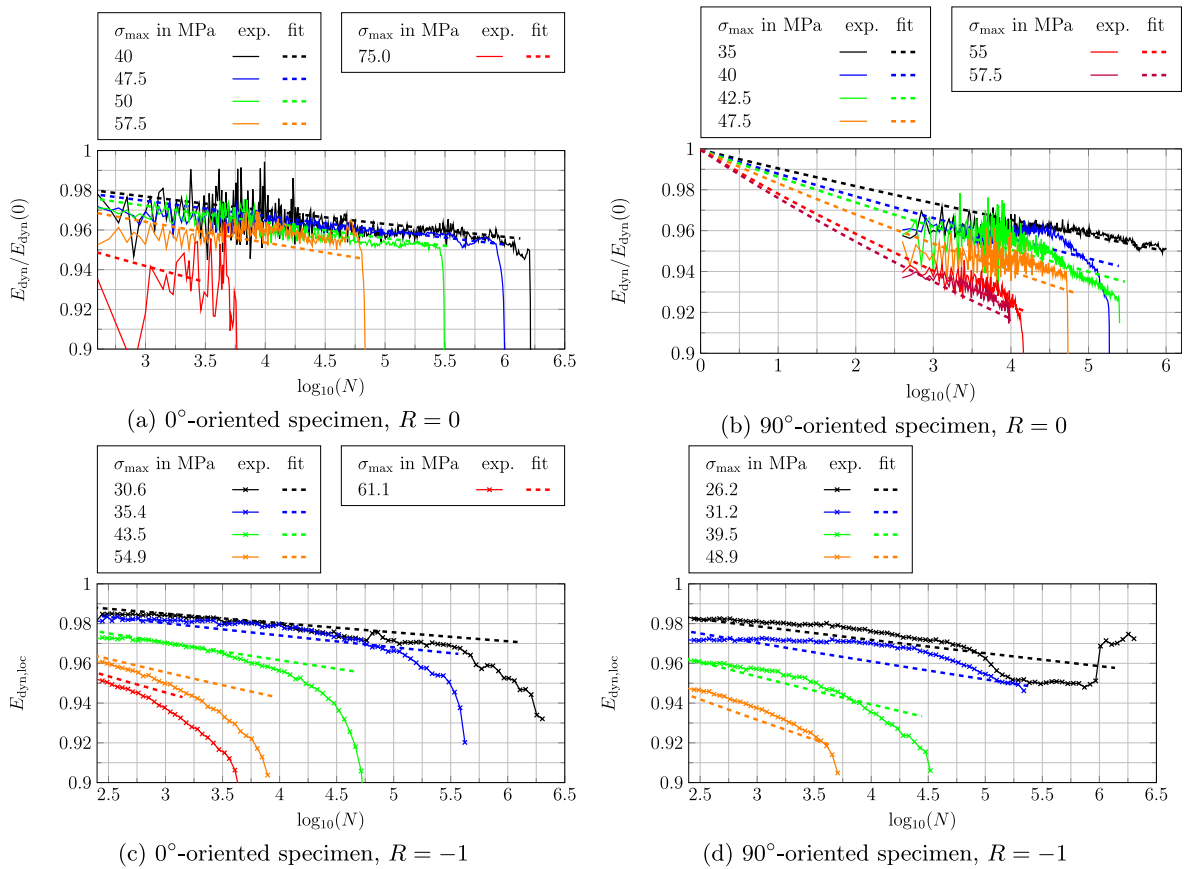


Fig. 20. Comparison of computational and experimental results for specimen B.

With increasing sharpness of the notch, the damage values at the notch increase as well. In contrast, the center of the specimen shows little damage. This observation does not come unexpected, as the stress peak in the notch drives the damage field via the evolution equation $\dot{D} = \alpha \sigma : \mathbb{S}_0 : \sigma$.

Due to the layered fiber-structure in the specimens, the fatigue-damage evolves non-uniformly over the specimen depth. In Fig. 18 the fatigue-damage is plotted for the 0°- and 90°-oriented specimen A. The loading cases are 47.5 MPa, $R = 0$ and 37.5 MPa, $R = 0$ at $N = 10^7$, respectively. We observe, that the maximum fatigue-damage in the 0°-

oriented specimens can be found in the surface layer, while the maximum fatigue-damage in the 90°-specimen is predicted in the center layer. This is due to the underlying microstructure: the maximum fatigue damage is predicted in the fiber layer, in which the most fibers are oriented in the loading direction. In the 0°-oriented specimen, the fibers in the approximately uniform outer fiber layers point in loading direction. In the 90°-oriented specimen these fibers point in the direction perpendicular to the loading direction. Thus for 90°-oriented specimens the approximately isotropic center layer is the layer with the most fibers pointing in loading direction.

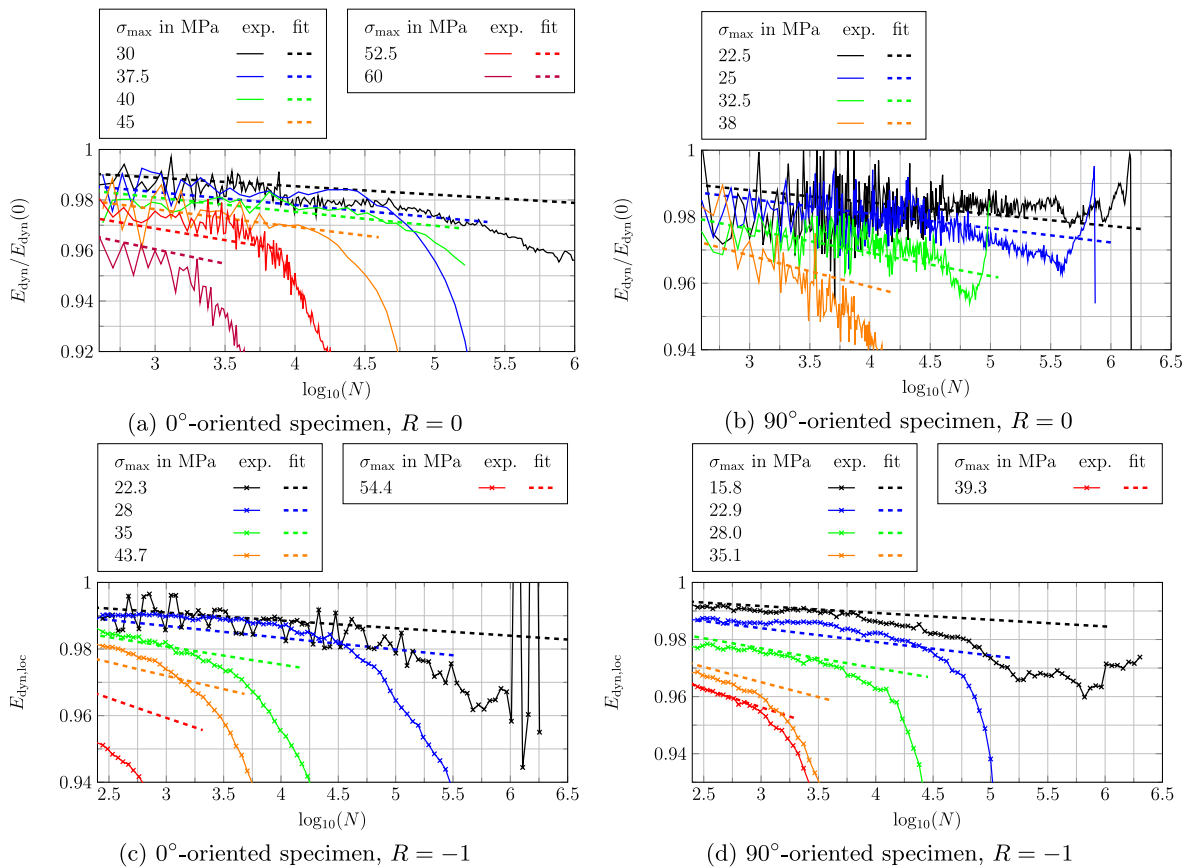


Fig. 21. Comparison of computational and experimental results for specimen C.

After these prestudies, we turn our attention to comparing the model predictions to experimental data. We first discuss the results for stress ratios of $R = -1$ for the unnotched specimen A. Experimental data and numerical predictions for specimens with fiber orientations of 0° and 90° are plotted in Fig. 19. For the 0° -oriented specimens shown in Fig. 19 (a), we observe a long and stable degradation phase of the material, which is roughly linear in logarithmic cycle space. For increasing loading amplitudes, i.e. for amplitudes σ_{max} larger than 72 MPa, we additionally observe a secondary fatigue-damage process with a more rapid decrease in the dynamic stiffness. This regime might be due to localizing fatigue cracks in the matrix, which we do not account for in the damage model at hand. The slope of the curve prior to this localizing regime is reproduced by the fatigue-damage model quite accurately. Recall that we did not use the experimental data at $R = -1$ to identify material parameters, but rather solely rely on experimental data for $R = 0$ for parameter identification.

For the 90° -oriented specimen, see Fig. 19(b), the non-linearity of the degradation curve increases. Yet, the fatigue-damage model is able to reproduce the stress-amplitude dependency in the stiffness degradation $\bar{N} = 0.5$ prior to failure.

We proceed with the discussion of experimental and numerical predictions for specimen B, shown in Fig. 20. The stiffness degradation of the material under loadings with a stress ratio of $R = 0$ are less nonlinear in the experiments than the stiffness degradation of specimens under loadings with a stress ratio of $R = -1$, where some curves tend towards a quadratic degradation when approaching a regime close to failure. This observation is in accordance with the data from specimen A. The experiments for $R = 0$ and $R = -1$ were conducted on different machines. $R = 0$ experiments ran on an Hähnchen system, whereas $R = -1$ ran on a Schenk system. This circumstance might also be one reason for the differences in the measurements. However, when focusing on the fatigue-damage regime with a linear slope, the simple damage model

captures the dependence on the orientation quite accurately. The largest deviations of the numerical predictions from the experimental data is found for experiments with $R = -1$ using 90° -oriented specimens at low stress amplitudes, shown in Fig. 20(d). In this setting, the experimental curves show a strongly non-linear behavior, which the numerical model does not reproduce. Yet, assuming that reproducing the linear trend in the data is of primary interest, the slope of the fatigue-damage model seems to be reasonable.

Finally, we compare experimental and computational predictions for the sharply notched specimen C in Fig. 21. The stiffness degradation for this specimen is in the range of 5%, which is half of the stiffness degradation observed in specimen B and about a quarter of the degradation observed in specimen A. This comes as no surprise, as the stress in the sharply notched specimen C is highly localized around the notch root. The majority of the part remains largely unaffected by fatigue damage. The overall stiffness degradation is thus smaller, yet noticeable. The linear fatigue-damage regime depending on R-value, orientation and stress amplitude is reproduced by the computational model with acceptable accuracy. The largest deviation observed when comparing experimental and numerical predictions for specimens C is found in the 0° -oriented, $R = -1$ -stress valued experiment with a maximum stress σ_{max} of 54.4 MPa. The stiffness loss in the experiment at $\bar{N} = 2.5$ is 5.17%, while a stiffness loss of 3.78% is predicted, which is a relative error of 19.5%. All other load cases studied, prior to localization and failure, remain well below this deviation. We conclude that the presented fatigue model is able to predict the stiffness loss in unnotched, mildly and sharply notched specimens subjected to stress amplitudes leading to fracture within the high cycle regime (10^3 - 10^6 cycles). The respective bearable load capacity depends on stress amplitude, stress ratio and orientation. Since the stress amplitude enters the damage evolution quadratically and is thus rather sensitive to its value, an extrapolation to other stress amplitudes should be handled with caution.

6. Conclusions

We proposed a special fatigue-damage model for the matrix material in short-fiber reinforced polymers formulated in time scale. This formulation enabled us to study the effect of fatigue damage during the first few cycles in detail. The proposed fatigue damage model is rather sensitive to the choice of parameters in the first few cycles, corresponding to the observation in experimental data that the dynamic modulus in the first few cycles scatters for different measurements. However, both material model and experimental data proved to be rather stable regarding the stiffness decrease in the high cycle regime.

To enable efficient computations in the high cycle regime, we proposed a cycle-jump technique building upon parametric loading curves. The parametrization of the loading curve enabled us to reformulate the model in terms of a cycle-scale and a logarithmic cycle-scale variable, respectively. Thus, the influence of load amplitude and mean stress can be consistently accounted for, while the computational efficiency is drastically increased compared to a pure time-scale based approach. The time-scale and cycle-scale models were studied and compared thoroughly. A combined time and cycle-scale approach (HLC) is suggested to combine the accuracy of the time-scale model in the first few cycles with the computational efficiency of the cycle-scale model in the high cycle regime.

Subsequently, the method was applied to model the fatigue damage behavior of a short-fiber reinforced polyamide. The material evolution was studied for different stress amplitudes, stress ratios, orientations and geometries. Using the data from 0°-oriented and 90°-oriented specimens for stress ratios of $R = 0$ to calibrate the material parameter α , the material behavior at different orientations, stress ratios and geometries can be predicted with reasonable accuracy.

In subsequent work, the investigation of a failure criterion remains an open question. Additionally, the scattering of the initial dynamic stiffness should be investigated more thoroughly. With a suitable failure criterion at hand, combined with the statistical influence of the initial stiffness, the prediction of Wöhler curves for short-fiber reinforced components is possible.

Credit authorship statement

Nicola Magino: Conceptualization; Evaluation of Experiments; Investigation; Software; Validation; Visualization; Writing - Original Draft. Jonathan Köbler: Software; Writing - Review & Editing. Heiko Andrä: Funding Acquisition; Project Administration; Supervision; Writing - Review & Editing. Fabian Welschinger: Investigation; Supervision of Experiments; Writing - Review & Editing. Ralf Müller: Supervision; Writing - Review & Editing. Matti Schneider: Conceptualization; Funding Acquisition; Project Administration; Supervision; Writing - Original Draft.

Declaration of competing interest

The authors declare that they have no known competing financial interests or personal relationships that could have appeared to influence the work reported in this paper.

Acknowledgements

MS acknowledges financial support of the German Research Foundation (DFG) within the International Research Training Group "Integrated engineering of continuous-discontinuous long fiber reinforced polymer structures" (GRK 2078). We are grateful to the anonymous reviewers, whose constructive remarks led to a significant improvement of the manuscript.

References

- [1] S. Mortazavian, A. Fatemi, Fatigue behavior and modeling of short fiber reinforced Polym Compos: a literature review, *Int. J. Fatig.* 70 (2015) 297–321.
- [2] J.L. Thomason, The influence of fibre properties of the performance of glass-fibre-reinforced polyamide 6,6, *Compos. Sci. Technol.* 59 (1999) 2315–2328.
- [3] G. Meneghetti, M. Ricotta, et al., An hysteresis energy-based synthesis of fully reversed axial fatigue behaviour of different polypropylene composites, *Compos. B* 65 (2014) 17–25.
- [4] N. Jia, V.A. Kagan, Effects of time and temperature on the tension-tension fatigue behavior of short fiber reinforced polyamides, *Polym. Compos.* 19 (1998) 408–414.
- [5] A. Hassan, N.A. Rahman, R. Yahya, Moisture absorption effect on thermal, dynamic mechanical and mechanical properties of injection-molded short glass-fiber/polyamide 6,6 composites, *Fibers Polym.* 13 (2012) 899–906.
- [6] M.F. Arif, F. Meraghni, et al., In situ damage mechanisms investigation of PA66/GF30 composite: effect of relative humidity, *Compos. B* 58 (2014) 487–495.
- [7] G. Meneghetti, M. Quaresimin, Fatigue strength assessment of a short fiber composite based on the specific heat dissipation, *Compos. B* 42 (2011) 217–255.
- [8] C.M. Sonsino, E. Moosbrugger, Fatigue design of highly loaded short-glass-fibre reinforced polyamide parts in engine compartments, *Int. J. Fatig.* 30 (2008) 1279–1288.
- [9] B. Klimkeit, B. Castagnet, et al., Fatigue damage mechanisms in short fiber reinforced PBT+PET GF30, *Mater. Sci. Eng.* 528 (2011) 1577–1588.
- [10] E. Chebbi, J. Mars, et al., Fatigue behavior of short glass fiber reinforced polyamide 66: experimental study and fatigue damage modelling, *Peri Poly. Mech. Eng.* 60 (4) (2016) 247–255.
- [11] M. de Monte, *Multiaxial Fatigue Behaviour of Short Fibre Reinforced Thermoplastics*, PhD thesis, Università di Bologna, 2008.
- [12] M. Amjadi, A. Fatemi, Multiaxial fatigue behavior of thermoplastics including mean stress and notch effects: experiments and modeling, *Int. J. Fatig.* 136 (2020) 105571.
- [13] A. Berrehili, S. Castagnet, Y. Nadot, Multiaxial fatigue criterion for a high-density polyethylene thermoplastic, *Fatig. Fract. Eng. Mater. Struct.* 33 (2010) 345–357.
- [14] A. Berrehili, Y. Nadot, et al., Multiaxial fatigue criterion for polypropylene – automotive applications, *Int. J. Fatig.* 32 (2010) 1389–1392.
- [15] G. Sines, Behavior of metals under complex static and alternating stresses, in: G. Sines, J.L. Waisman (Eds.), *Metal Fatigue*, 145–169, McGraw-Hill Book Co., New York, 1959.
- [16] B. Crossland, Effect of large hydrostatic pressures on the torsional fatigue strength of an alloy steel, in: *International Conference on Fatigue of Metals*, 1956, p. 13849.
- [17] J. Zhang, H. Jiang, et al., A new form of equivalent stress for combined axial-torsional loading considering the tension-compression asymmetry of polymeric materials, *RSC Adv.* 5 (89) (2015) 72780–72784.
- [18] A. Launay, M.H. Maitoïnam, et al., Multiaxial fatigue models for short glass fiber reinforced polyamide – Part I: nonlinear anisotropic constitutive behavior for cyclic response, *Int. J. Fatig.* 47 (2013) 382–389.
- [19] A. Launay, M.H. Maitoïnam, et al., Multiaxial fatigue models for short glass fibre reinforced polyamide. Part II: fatigue life estimation, *Int. J. Fatig.* 47 (2013) 390–406.
- [20] B. Klimkeit, Y. Nadot, et al., Multiaxial fatigue life assessment for reinforced polymers, *Int. J. Fatig.* 33 (2011) 766–780.
- [21] A. Zago, G. Springer, Fatigue lives of short fiber reinforced thermoplastics parts, *J. Reinforc. Plast. Compos.* 20 (7) (2001) 606–620.
- [22] M. de Monte, E. Moosbrugger, et al., Multiaxial fatigue of a short glass fibre reinforced polyamide 6.6 – fatigue and fracture behaviour, *Int. J. Fatig.* 32 (2010) 17–28.
- [23] M. de Monte, E. Moosbrugger, M. Quaresimin, Influence of temperature and thickness on the off-axis behaviour of short glass fibre reinforced polyamide 6.6 – cyclic loading, *Compos. A* 41 (10) (2010) 1368–1379.
- [24] Y. Zhou, P.K. Mallick, Fatigue performance of an injection-moulded short E-glass fiber-reinforced polyamide 6,6. I. Effects of orientation, holes and weld line, *Polym. Compos.* 27 (2) (2006) 230–237.
- [25] A. Bernasconi, E. Conrado, P. Hene, An experimental investigation of the combined influence of notch size and fibre orientation on the fatigue strength of a short glass fibre reinforced polyamide 6, *Polym. Test.* 47 (2015) 12–21.
- [26] L.M. Kachanov, Rupture time under creep conditions, *Int. J. Fract.* 97 (1999) 11–18.
- [27] J. Lemaitre, A continuous damage mechanics model for ductile fracture, *J. Eng. Mater. Technol.* 107 (1) (1985) 83–89.
- [28] R. Desmorat, *Continuum Damage Mechanics Modeling for Fatigue of Materials and Structures*, vol. 10, *Révue Européenne de Génie Civil*, 2006, pp. 849–877.
- [29] A. Djebbi, M. Bendouba, et al., Experimental Analysis and Damage Modeling of high-density polyethylene under fatigue loading, *Acta Mech. Solida Sin.* 29 (2) (2016) 133–144.
- [30] E. Chebbi, J. Mars, et al., A new cumulative fatigue damage model for short glass fiber-reinforced polyamide 66, in: M. Haddar, F. Chaari, A. Benamara, M. Chouchane, C. Karra, N. Aifaoui (Eds.), *Design and Modeling of Mechanical Systems—III*, Springer, Cham, 2018, pp. 227–234.
- [31] R. Billardon, *Etude de la rupture par la mécanique de l'endommagement*. PhD thesis, Université Paris 6 (2011).
- [32] J. Lemaitre, I. Doghri, Damage 90: a post processor for crack initiation, *CMAME* 115 (1994) 197–232.
- [33] W. Van Paeppegem, J. Degrieck, P. De Baets, Finite element approach for modelling fatigue damage in fibre-reinforced composite materials, *Compos. B* 32 (2001) 575–588.

- [34] A. Turon, J. Costa, et al., Simulation of delamination in composites under high-cycle fatigue, *Compos. A* 38 (2007) 2270–2282.
- [35] O. Sally, F. Laurin, et al., An efficient computational strategy of cycle-jumps dedicated to fatigue of composite structures, *Int. J. Fatig.* 135 (2020) 1–14, 105500.
- [36] T. Titscher, J. Unger, Efficient higher-order cycle jump integration of a continuum fatigue damage model, *Int. J. Fatig.* 141 (2020) 105863.
- [37] A. Bhattacharyya, D. Dureisseix, B. Faverjon, A unified approach based on temporal homogenisation and cycle jump for thermo-mechanical combined cycle fatigue, *Int. J. Fatig.* 131 (2020) 105320.
- [38] J.-Y. Cognard, P. Ladevèze, A large time increment approach for cyclic viscoplasticity, *Int. J. Plast.* 9 (1993) 141–157.
- [39] M. Bhattacharyya, A. Fau, et al., A kinetic two-scale damage model for high-cycle fatigue simulation using multi-temporal Latin framework, *Europ. J. Mech./A* 77 (2019) 103808.
- [40] F. Chinesta, A. Ammar, et al., An overview of the proper generalized decomposition with applications in computational rheology, *J. Non-Newtonian Fluid Mech.* 166 (2011) 578–592.
- [41] P. Ladevèze, J.-C. Passieux, D. Néron, The Latin multiscale computational method and the proper generalized decomposition, *CMAME* 199 (2010) 1287–1296.
- [42] Q. Yu, J. Fish, Temporal homogenization of viscoelastic and viscoplastic solids subjected to locally periodic loading, *Comput. Mech.* 29 (3) (2002) 199–211.
- [43] G. Puel, D. Aubry, Material fatigue simulation using a periodic time-homogenisation method, *Europ. J. Com. Mech.* 21 (3–6) (2012) 312–324.
- [44] H. Altenbach, D. Breslavsky, et al., Two-time-scales and time-averaging approaches for the analysis of cyclic creep based on Armstrong–Frederick type constitutive model, *J. Mech. Eng. Sci.* 233 (5) (2018) 1690–1700.
- [45] A. Devulder, D. Aubry, G. Puel, Two-time-scale fatigue modelling: application to damage, *Comput. Mech.* 45 (6) (2010) 637–646.
- [46] H. Moulinec, P. Suquet, A fast numerical method for computing the linear and nonlinear mechanical properties of composites, *Comptes Rendus de l'Académie des Sciences. Série II* 318 (11) (1994) 1417–1423.
- [47] J. Kochmann, S. Wulfinghoff, et al., Two-scale FE–FFT- and phase-field-based computational modeling of bulk microstructural evolution and macroscopic material behavior, *CMAME* 305 (2016) 89–110.
- [48] J. Spahn, H. Andrä, et al., A multiscale approach for modeling progressive damage of composite materials using fast fourier transforms, *CMAME* 268 (2014) 871–883.
- [49] G.J. Dvorak, Transformation field analysis of inelastic composite materials, *Proc. Math. Phys. Sci.* 437 (1900) (1992) 311–327.
- [50] J.C. Michel, P. Suquet, Nonuniform transformation field analysis, *Int. J. Solid Struct.* 40 (25) (2003) 6937–6955.
- [51] F. Fritzen, M. Leuschner, Reduced basis hybrid computational homogenization based on a mixed incremental formulation, *CMAME* 260 (2013) 143–154.
- [52] J. Köbler, N. Magino, et al., A computational multi-scale model for the stiffness degradation of short-fiber reinforced plastics subjected to fatigue loading, *CMAME* 373 (2021) 113522.
- [53] Z. Liu, C.T. Wu, M. Koishi, A deep material network for multiscale topology learning and accelerated nonlinear modeling of heterogeneous materials, *CMAME* 345 (2019) 1138–1168.
- [54] Z. Liu, H. Wei, et al., Intelligent Multiscale Simulation Based on Process-Guided Composite Database, *arXiv e-prints*, 2020, pp. 1–15, 2003.09491.
- [55] S. Gajek, M. Schneider, T. Böhlke, On the micromechanics of deep material networks, *J. Math. Phys. Solid* 142 (2020) 103984.
- [56] S. Gajek, M. Schneider, T. Böhlke, An FE–DMN method for the multiscale analysis of short fiber reinforced plastic components, *CMAME* 384 (2021) 113952.
- [57] J. Görthofer, M. Schneider, et al., A convex anisotropic damage model based on the compliance tensor, *Int. J. Damage Mech.* (2022) 43–86. Online.
- [58] A. Jain, J.M. Veas, et al., The Master SN curve approach – a hybrid multi-scale fatigue simulation of short fiber reinforced composites, *Compos. A* 91 (2016) 510–518.
- [59] M.H.J.W. Paas, P.J.G. Schreurs, W.A.M. Brekelmans, A continuum approach to brittle and fatigue damage: theory and numerical procedures, *Int. J. Solid Struct.* 30 (1993) 579–599.
- [60] R.H.J. Peerlings, W.A.M. Brekelmans, et al., Gradient-enhanced damage modelling of high-cycle fatigue, *Int. J. Numer. Methods Eng.* 49 (2000) 1547–1569.
- [61] N. Magino, J. Köbler, et al., A multiscale high-cycle fatigue-damage model for the stiffness degradation of fiber-reinforced materials based on a mixed variational framework, *CMAME* 388 (2022) 114198.
- [62] J.L. Chaboche, Continuum damage mechanics: present state and future trends, *Nucl. Eng. Des.* 105 (1987) 19–33.
- [63] J. Görthofer, M. Schneider, et al., A convex anisotropic damage model based on the compliance tensor, *Int. J. Damage Mech.* 31 (1) (2022).
- [64] J. Lemaître, R. Desmorat, *Engineering Damage Mechanics – Ductile, Creep, Fatigue and Brittle Failures*, Springer, Berlin Heidelberg, 2015.
- [65] A.S.J. Suiker, R. de Borst, A numerical model for the cyclic deterioration of railway tracks, *Int. J. Numer. Methods Eng.* 57 (2003) 441–470.
- [66] R. Largeton, J.-C. Michel, P. Suquet, Extension of the Nonuniform Transformation Field Analysis to linear viscoelastic composites in the presence of aging and swelling, *Mech. Mater.* 73 (2014) 76–100.
- [67] H. Altenbach, *Kontinuumsmechanik – Einführung in die materialunabhängigen und materialabhängigen Gleichungen*, Springer, Berlin Heidelberg, 2015.
- [68] M. Fremond, B. Nedjar, Damage, gradient of damage, and principle of virtual power, *Int. J. Solid Struct.* 33 (1996) 1083–1103.
- [69] R.H.J. Peerlings, R. de Borst, et al., Some observations on localisation in non-local and gradient damage models, *Europ. J. Mech. A* 15 (1996) 937–953.
- [70] R.H.J. Peerlings, R. de Borst, et al., Gradient-enhanced damage modelling of concrete fracture, *Mech. Coh-Fric Mat* 3 (1998) 323–342.
- [71] C. Lüders, M. Sinapius, D. Krause, Adaptive cycle jump and limits of degradation in micromechanical fatigue simulations of fibre-reinforced plastics, *Int. J. Damage Mech.* 28 (10) (2019).
- [72] P. Ladevèze, An anisotropic damage theory with unilateral effects: application to laminates and to three- and four-dimensional composites, in: O. Allix, F. Hild (Eds.), *Cont. Dam. Mech. Mat. Struct.*, 205–233, Elsevier Science, Oxford, 2002.
- [73] P. Ladevèze, A. Gasser, O. Allix, Damage mechanisms modeling for ceramic composites, *J. Eng. Mater. Technol.* 116 (1994) 331–336.
- [74] M.F. Arif, F. Meraghni, et al., Multiscale fatigue damage characterization in short glass fiber reinforced polyamide-66, *Compos. B* 61 (2014) 55–65.
- [75] J. Schijve, *Fatigue under Variable-Amplitude Loading*, Springer Netherlands, Dordrecht, 2009, pp. 295–328.
- [76] P.R. Vieira, E.M.L. Carvalho, et al., Experimental fatigue behavior of pultruded glass fibre reinforced polymer composite materials, *Compos. B* 146 (2018) 69–75.
- [77] M. Kawai, H. Takeuchi, et al., Effects of temperature and stress ratio on fatigue life of injection molded short carbon fiber-reinforced polyamide composite, *Compos. A* 98 (2017) 9–24.
- [78] P.B.S. Bailey, M. Highman, Application of strain-controlled fatigue testing methods to polymer matrix composites, *Procedia Struct. Integrity* 2 (2016) 128–135.
- [79] B. Halphen, Q.S. Nguyen, Sur les matériaux standards généralisés, *J. Mec.* 14 (1975) 508–520.
- [80] P.S. Nguyen, *Stability and Nonlinear Solid Mechanics*, Wiley, New York, 2000.
- [81] P.A. Hessman, F. Welschinger, et al., On mean field homogenization schemes for short fiber reinforced composites: unified formulation, application and benchmark, *Int. J. Solid Struct.* 230–231 (2021) 111141.
- [82] P.A. Hessman, T. Riedel, et al., Microstructural analysis of short glass fiber reinforced thermoplastics based on x-ray micro-computed tomography, *Compos. Sci. Technol.* 183 (2019) 107752.
- [83] J. Köbler, M. Schneider, et al., Fiber orientation interpolation for the multiscale analysis of short fiber reinforced composite parts, *Comput. Mech.* 61 (2018) 729–750.
- [84] *FeelMath, FeelMath, Fraunhofer Institute for Industrial Mathematics, Kaiserslautern, Germany, 2021.* <http://www.itwm.fraunhofer.de/en/fraunhofer-itwm.html>.
- [85] M. Schneider, The Sequential Addition and Migration method to generate representative volume elements for the homogenization of short fiber reinforced plastics, *Comput. Mech.* 59 (2017) 247–263.
- [86] M. Schneider, F. Ospald, M. Kabel, Computational homogenization of elasticity on a staggered grid, *Int. J. Numer. Methods Eng.* 105 (9) (2016) 693–720.
- [87] M. Kabel, T. Böhlke, M. Schneider, Efficient fixed point and Newton–Krylov solvers for FFT-based homogenization of elasticity at large deformations, *Comput. Mech.* 54 (2014) 1497–1514.
- [88] Z. Mouti, K. Westwood, et al., Finite element analysis of glass fiber-reinforced polyamide engine oil Pan subjected to localized low velocity impact from flying projectiles, *Steel Res. Int.* 83 (10) (2012) 957–963.
- [89] S.G. Advani, C.L. Tucker, The use of tensors to describe and predict fiber orientation in short fiber composites, *J. Rheol.* 31 (8) (1987) 751–784.
- [90] *Abaqus/Standard, Dassault Systèmes Simulia.* <https://www.3ds.com/product-s-services/simulia/products/abaqus/>. (Accessed 19 October 2021).